

<https://doi.org/10.1038/s42004-024-01224-0>

Development of Nurr1 agonists from amodiaquine by scaffold hopping and fragment growing

Check for updates

Minh Sai¹, Emily C. Hank¹, Hin-Man Tai², Till Kasch¹, Max Lewandowski¹, Michelle Vincendeau^{2,3}, Julian A. Marschner¹ & Daniel Merk¹ ✉

The neuroprotective transcription factor nuclear receptor-related 1 (Nurr1) has shown great promise as a therapeutic target in Parkinson's and Alzheimer's disease as well as multiple sclerosis but high-quality chemical tools for pharmacological target validation of Nurr1 are rare. We have employed the weak Nurr1 modulator amodiaquine (AQ) and AQ-derived fragments as templates to design a new Nurr1 agonist chemotype by scaffold hopping and fragment growing strategies. Systematic structural optimization of this scaffold yielded Nurr1 agonists with nanomolar potency and binding affinity. Comprehensive *in vitro* profiling revealed efficient cellular target engagement and compliance with the highest probe criteria. In human midbrain organoids bearing a Parkinson-driving LRRK2 mutation, a novel Nurr1 agonist rescued tyrosine hydroxylase expression highlighting the potential of the new Nurr1 modulator chemotype as lead and as a chemical tool for biological studies.

Nuclear receptor related 1 (Nurr1, NR4A2) is a ligand-activated transcription factor mainly expressed in neurons and immune cells of the brain^{1–3}. The receptor is critically involved in the regulation of (dopaminergic) neuron development and maintenance as well as inflammatory processes^{3–6}. Observations of diminished Nurr1 levels in patients⁷ and animal models^{8–10} of Alzheimer's (AD) and Parkinson's diseases (PD) underline the therapeutic potential of Nurr1 activation in neurodegenerative diseases. Moreover, recent findings suggest a protective and anti-inflammatory role of Nurr1 in retinal pigment epithelial cells in the eye with possible therapeutic relevance in age-related macular degeneration¹¹. Pharmacological activation of Nurr1 may therefore offer new therapeutic options in various degenerative diseases and potent Nurr1 agonists are needed¹².

Nurr1 acts as a monomer, homodimer, or heterodimer and has constitutive transcriptional activator activity also in the absence of ligands but can be modulated by agonists and inverse agonists in a bidirectional fashion^{13–15}. The dopamine metabolite 5,6-dihydroxyindole (DHI)¹⁶, polyunsaturated fatty acids¹⁷ and the prostaglandins A and E¹⁸ have been identified as natural Nurr1 ligands. A few synthetic Nurr1 ligand chemotypes have been recently identified^{19–23} among which the antimalarial amodiaquine (AQ; Fig. 1; EC₅₀~20 μM)²⁴ was the first validated Nurr1 agonist and emerged as an early tool to study therapeutic effects of Nurr1 activation²⁴. AQ treatment counteracted neuroinflammation and ameliorated behavioral deficits in a PD model²⁴, and reduced neuronal loss and amyloid-beta deposition in an AD model²⁵. However, while offering access

to Nurr1 ligand discovery, AQ is unspecific^{19,26–28} and hepatotoxic²⁹, and pharmacological effects with AQ cannot confidently be assigned to Nurr1 modulation. For example, AQ was found to inhibit autophagy, stabilize p53, block ribosome biogenesis, suppress PPARγ induced adipogenesis, and cause endoplasmic reticulum stress^{30–33} thus affecting multiple cellular processes. Moreover, AQ and many analogues contain pan-assay interference compounds (PAINS)^{34,35} elements further compromising their value as a chemical tool. Therefore, AQ descendants with improved potency and selectivity are needed to validate the promising observations on Nurr1-mediated therapeutic effects of this drug. So far, structural optimization efforts have yielded the AQ descendant **1** exhibiting improved Nurr1 agonist potency and protective effects in a PD model³⁶, simplified 7-chloroquinolin-4-amine (**2**) and 8-chloro-2-methylquinolin-4-amine (**3**) fragments with enhanced Nurr1 agonism²⁸, and a 5-(4-chlorophenyl)furan-2-carboxamide motif (**4**)³⁷ as replacement for the unfavorable 4-aminophenol residue of AQ.

Here, we aimed to develop AQ-derived Nurr1 agonists to enable target validation studies on the promising effects of AQ in neurodegeneration. Systematic optimization, scaffold-hopping, and fusion of AQ substructures yielded a next-generation Nurr1 ligand scaffold offering high potency and selectivity. Comprehensive characterization and validation demonstrated high affinity binding to Nurr1, cellular target engagement, low toxicity, favorable permeability, and tunable metabolic stability. A potent and extensively validated Nurr1 agonist of the AQ-derived chemotype and a structurally matched

¹Ludwig-Maximilians-Universität München, Department of Pharmacy, 81377 Munich, Germany. ²Helmholtz Munich, Institute of Virology, 85764 Munich, Germany.

³Technical University of Munich, Institute of Virology, School of Medicine, 81675 Munich, Germany. ✉e-mail: daniel.merk@cup.lmu.de

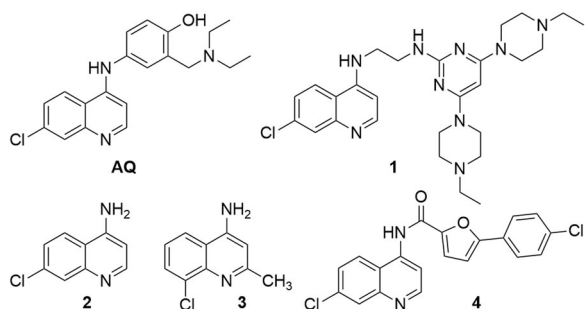


Fig. 1 | Nurr1 agonists. Amodiaquine (AQ)²⁴, the optimized AQ derivative **1**³⁶, the AQ-derived fragments **2** and **3**²⁸, and the AQ derivative **4** from microscale combinatorial chemistry³⁷.

negative control compound together provide a high-quality chemical tool for biological studies to validate Nurr1-dependent pharmacological effects of AQ and advance Nurr1 modulation as a therapeutic concept.

Results & Discussion

Design and structural optimization of Nurr1 agonists

Antimalarial activity of AQ and related compounds is mainly ascribed to the common chloroquinoline scaffold present in several antimalarials³⁸ while the 4-hydroxyaniline is considered mainly responsible for cyto- and hepatotoxicity after metabolic activation to a reactive quinoneimine^{29,32}. Additionally, cellular AQ effects, e.g., on autophagy and p53, surpassed the activity of chloroquinone (CQ)^{30,31} which is structurally related but lacks the 4-aminophenol moiety indicating that this substructure also mediates off-target activities of AQ.

Optimization of the AQ scaffold for Nurr1 agonism hence demanded the replacement of both the chloroquinolineamine and 4-aminophenol motifs. As we have previously found that 7-chloroquinoline-4-amine (**2**) is sufficient for Nurr1 activation and can be tuned in Nurr1 agonism by variation of its substitution pattern²⁸, we aimed for optimization of the chloroquinolineamine fragment by scaffold hopping and subsequent fragment extension. Thus, we commenced the development of AQ-derived Nurr1 modulators by probing replacement of the quinoline scaffold of the optimized AQ fragment **3** by alternative heterocycles (Table 1). The corresponding quinazoline **5** was inactive and 7-chloro-2-methyl-1H-indol-3-amine (**6**) was not stable. 4-Chloro-2-methyl-benzimidazole (**7**) also failed to activate Nurr1 suggesting that the amino substituent was required and could not be replaced by the ring NH.

The alternative imidazo[1,2-*a*]pyridine scaffold (**8**), in contrast, retained Nurr1 agonism and achieved a notable improvement in potency and efficacy compared to **4**. The smaller skeleton was not compatible with the original regiochemistry of the chloro substituent (**9**) and systematic deconstruction of **8** indicated a tight SAR with the importance of all substituents (**10–13**). Despite weak to no Nurr1 activation by **9–13**, isothermal titration calorimetry (ITC, Table 1, Supplementary Fig. 1) demonstrated that **11** and **12** containing the 8-chloro substituent still bound with low micromolar affinity to the Nurr1 LBD while **10** and **13** lacking the chlorine atom exhibited weaker binding. These results thus highlighted the 8-chloro substituent as a key factor driving affinity and the amino motif as relevant for Nurr1 activation. With single-digit micromolar potency (EC_{50} 7 μ M) and affinity (K_d 2.7 μ M, Fig. 2a), 8-chloro-2-methylimidazo[1,2-*a*]pyridine (**8**) emerged as an improved fragment-like Nurr1 agonist which was also evident from enhanced ligand efficiency (LE), lipophilic ligand efficiency (LLE), and size-independent ligand efficiency (SILE) compared to AQ and the lead fragment **3** (Table 2).

Imidazopyridine-based NR4A modulators have been reported previously^{39–41}, but independent evaluation by Munoz-Tello et al.¹⁹ provided no evidence for binding of a selected example of this chemotype (SR24237)⁴⁰ to Nurr1. For direct comparison, we profiled the previously reported imidazopyridine-based Nurr1 agonist SA00025 (EC_{50} (NBRE) 0.217 μ M)³⁹

Table 1 | Optimization of the chloroquinoline fragment

ID	structure	EC_{50} (Nurr1) (max. activation) ^a	K_d (Nurr1 LBD) ^b
3		17 \pm 6 μ M (1.7 \pm 0.1-fold)	n.d.
5		inactive (100 μ M)	n.d.
6		unstable	n.d.
7		inactive (100 μ M)	n.d.
8		7 \pm 1 μ M (2.0 \pm 0.1-fold)	2.7 μ M
9		inactive (100 μ M)	weak binding
10		inactive (100 μ M)	weak binding
11		inactive (100 μ M)	7.2 μ M
12		< 1.2-fold activation	5.1 μ M
13		inactive (100 μ M)	weak binding

^aNurr1 modulation was determined in a Gal4-Nurr1 hybrid reporter gene assay. Max. activation refers to the maximum effect vs. 0.1% DMSO control. Data are the mean \pm SD; $n \geq 3$. ^b K_d values were determined by isothermal titration calorimetry (cf. Fig. 2a Supplementary Fig. 1). n.d. - not determined; weak binding - titration of 15 μ M Nurr1 with 100 μ M ligand showed heat differences indicative of binding that could not be fitted, however.

in our test systems (refer to Supplementary Fig. 2 for assay setups; chemical structure and data for SA00025 in Supplementary Fig. 3). No activation of Nurr1 (or the related NR4A receptors Nur77 and NOR1) by SA00025 was detectable in the Gal4-hybrid reporter gene assay in the concentration range from 10 nM to 3 μ M (Supplementary Fig. 3b). At higher concentration, SA00025 was considerably cytotoxic. As literature³⁹ reported activation of full-length human Nurr1 by SA00025 on the NBRE response element, we also employed reporters for the human Nurr1 response elements (NBRE, NurRE, DR5)¹⁴ but detected no effect of SA00025 (Supplementary Fig. 3c). Orthogonal evaluation of SA00025 in cell-free setting by ITC indicated potential weak binding, but insufficient affinity to determine a K_d value with this technique (Supplementary Fig. 3d). In accordance with the findings of Munoz-Tello et al.¹⁹, these results do not support potent Nurr1 agonism of

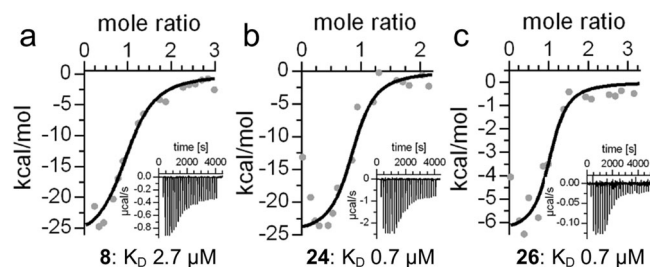


Fig. 2 | Orthogonal validation of ligand binding to Nurr1 by isothermal titration calorimetry (ITC). The fittings of the heat of binding are shown for **8** (a), **24** (b), and **26** (c) and the isotherms at 25 °C are shown as insets.

Table 2 | Ligand efficiency metrics of 1, 4, 8, 24, 26 and 36.^a

	1	4	8	24	26	36
pEC ₅₀	4.7	4.8	5.2	6.4	5.8	7.0
LE	0.26	0.50	0.59	0.46	0.31	0.34
LLE	-0.48	1.99	3.28	1.86	0.34	2.18
SILE	1.79	2.21	2.45	2.64	2.18	2.59

^aLigand efficiency (LE), lipophilic ligand efficiency (LLE), and size-independent ligand efficiency (SILE) were computed according to ref. 62.

SA00025 and related compounds and align with the lack of activity of **9** indicating that 8-substituted imidazopyridines like **8** are favored over analogues with substituents in 7-position.

Aiming to enhance potency by fragment growing, we next evaluated a potential optimization of the 2-methyl substituent of **8** (Table 3). Extension in this region caused a general reduction in Nurr1 activation efficacy. In a rough exploration of aliphatic (**14**) and aromatic (**15**, **16**) extensions, only the phenyl substituent (**15**) retained sufficient efficacy and provided a slight improvement over **8** in terms of potency (EC₅₀ 4 μM). Chloro substituents in 4- (**17**) and 3- (**18**) positions of the phenyl motif enhanced activation efficacy but diminished potency. 2-Chloro substitution (**19**) disrupted activity on Nurr1. Replacement of the chloro substituents (**17**, **18**) by a methyl group was tolerated in 4-position (**20**) but not in 3-position (**21**), and trifluoromethyl substituents (**22**, **23**) also caused a marked drop in efficacy. Double 3,4-chloro substitution (**24**), in contrast, was additive and resulted in enhanced potency (EC₅₀ 0.4 μM) and efficacy (1.8-fold activation). The corresponding dimethyl analogue **25** was less active.

Structural extension of the 2-methyl substituent in **8** thus provided no major gain in Nurr1 agonist activity. Only the 3,4-dichlorophenyl derivative **24** achieved a notable increase in potency over **8** which was in line with results from ITC confirming enhanced affinity of **24** (K_d 0.7 μM, Fig. 2b). In terms of ligand efficiency (Table 2), the structural extension from **8** to **24** represented no significant improvement but the 2-(3,4-dichlorophenyl) substituent of **24** may still be a valuable potency driving extension in fused derivatives.

The optimized Nurr1 agonist **8** obtained by fragment hopping from the chloroquinoline motif of AQ also appeared suitable for fragment growing by fusion with N-substituents. Our previous studies³⁷ have revealed a 5-(4-chlorophenyl)furan-2-carboxamide residue as alternative motif to replace the aminophenol of AQ. Transfer of this SAR knowledge to the new imidazo[1,2-*a*]pyridine scaffold of **8** in the fused 5-(4-chlorophenyl)furan-2-carboxamide derivative **26** provided an improvement in Nurr1 agonist potency (Table 4) but decreased ligand efficiency (Table 2). Simplification of **26** by removal of the chloro substituent (**27**) was tolerated but among alternative central aromatic systems, only thiophene (**28**) retained Nurr1 agonism. Replacement of furan (**27**) by pyrrole (**29**) or benzene (**30**) disrupted activity thus suggesting **26** as lead for further optimization which was also supported by improved binding affinity of **26** (K_d 0.7 μM, Fig. 2c). Further optimization potential seemed to rest in the 4-chloro substituent as its removal (**27**) hardly diminished potency. This indicated that space to accommodate substituents was

Table 3 | Extension of the imidazo[1,2-*a*]pyridine **8**

ID		EC ₅₀ (Nurr1) (max. activation) ^a
8		7 ± 1 μM (2.0 ± 0.1-fold)
14		< 1.2-fold act.
15		4 ± 2 μM (1.4 ± 0.1-fold)
16		< 1.2-fold act.
17		15 ± 3 μM (1.7 ± 0.2-fold)
18		9 ± 3 μM (1.7 ± 0.1-fold)
19		inactive (100 μM)
20		12 ± 2 μM (2.0 ± 0.2-fold)
21		< 1.2-fold act.
22		< 1.2-fold act.
23		< 1.2-fold act.
24		0.4 ± 0.2 μM (1.8 ± 0.1-fold)
25		14 ± 2 μM (1.6 ± 0.1-fold)

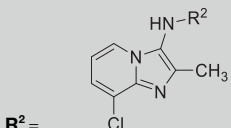
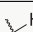
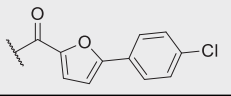
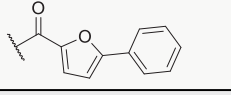
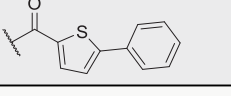
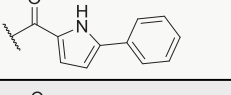
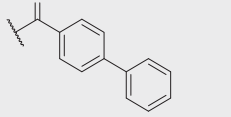
^aNurr1 modulation was determined in a Gal4-Nurr1 hybrid reporter gene assay. Max. activation refers to the maximum effect vs. 0.1% DMSO control. Data are the mean ± SD; n ≥ 3.

available in this region and we thus focused our attention on alternative motifs to replace the chlorine atom as 4-substituent of the phenylfuran-2-carboxamide residue (Table 5).

The 4-trifluoromethyl derivative **31** exhibited similar activity as **26** while the corresponding 4-methyl analogue **32** was substantially more potent. A similar trend was observed for the 4-trifluoromethoxy (**33**) and 4-methoxy (**34**) pair, which indicated the potential relevance of inductive effects. Like 4-methyl (**32**) and 4-methoxy (**34**), a 4-methylamino substituent (**35**) was highly favored and enhanced Nurr1 agonist potency to a sub-micromolar range. A 4-dimethylamino group (**36**) provided a further improvement to a double-digit nanomolar EC₅₀ value.

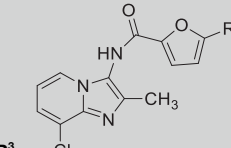
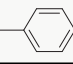
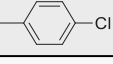


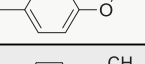

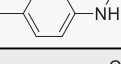
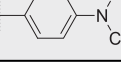
The SAR evaluation had revealed favorable contributions to Nurr1 agonist potency for a 3,4-dichlorophenyl substituent in 2-position of the imidazopyridine scaffold (**24**) and for the 5-(4-(dimethylamino)phenyl)furan-2-carboxamide motif in 3-position (**36**). Structural fusion of these modifications in the combined derivative **37** (Fig. 3) generated a high-affinity Nurr1 modulator (K_d 0.08 μM, Supplementary Fig. 4) with strong agonist potency (EC₅₀ = 0.04 ± 0.01 μM), but the fused compound **37** did

Table 4 | Fusion of 8 with N-substituents

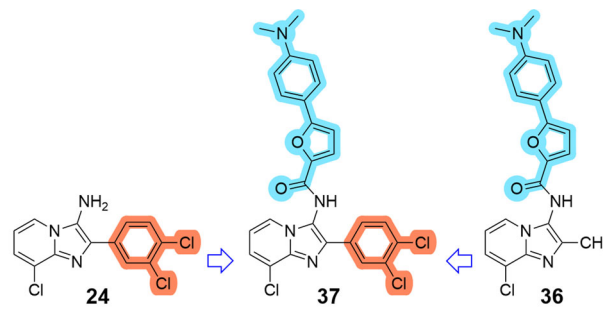
ID	 R ² =	EC ₅₀ (Nurr1) (max. activation) ^a
8		7 ± 1 μM (2.0 ± 0.1-fold)
26		1.6 ± 0.5 μM (1.8 ± 0.1-fold)
27		4 ± 1 μM (2.1 ± 0.1-fold)
28		3.2 ± 0.4 μM (2.1 ± 0.1-fold)
29		inactive (10 μM ^b)
30		inactive (10 μM ^b)

^aNurr1 modulation was determined in a Gal4-Nurr1 hybrid reporter gene assay. Max. activation refers to the maximum effect vs. 0.1% DMSO control. Data are the mean ± SD; *n* ≥ 3. ^bHighest non-toxic concentration.

Table 5 | Optimization of the fused derivative 26

ID	 R ³ =	EC ₅₀ (Nurr1) (max. activation) ^a
27		4 ± 1 μM (2.1 ± 0.1-fold)
26		1.6 ± 0.5 μM (1.8 ± 0.1-fold)
31		1.1 ± 0.3 μM (1.8 ± 0.1-fold)
32		0.13 ± 0.02 μM (2.0 ± 0.2-fold)
33		0.8 ± 0.2 μM (2.0 ± 0.1-fold)
34		0.16 ± 0.06 μM (1.7 ± 0.1-fold)
35		0.30 ± 0.02 μM (1.8 ± 0.1-fold)
36		0.090 ± 0.005 μM (2.1 ± 0.1-fold)

^aNurr1 modulation was determined in a Gal4-Nurr1 hybrid reporter gene assay. Max. activation refers to the maximum effect vs. 0.1% DMSO control. Data are the mean ± SD; *n* ≥ 3.



EC ₅₀	0.4 ± 0.2 μM	0.04 ± 0.01 μM	0.090 ± 0.005 μM
eff.	1.8 ± 0.1-fold	1.53 ± 0.04-fold	2.1 ± 0.1-fold
K _d	0.7 μM	0.08 μM	0.17 μM

Fig. 3 | Structural fusion of 24 and 36 in 37 enhanced Nurr1 agonist potency and binding affinity. Nurr1 modulation was determined in a Gal4-Nurr1 hybrid reporter gene assay. Max. activation refers to the maximum effect vs. 0.1% DMSO control. Data are the mean ± SD; *n* ≥ 3. Binding affinity was determined by ITC.

not substantially outmatch 36 and was significantly more lipophilic (37: SlogP 7.54).

Biological profiling of the Nurr1 agonist 36

These results highlighted 36 as preferred Nurr1 agonist from the scaffold hopping and fragment growing approach. Potent Nurr1 agonism of 36 was also evident in reporter gene assays to observe the activity of the full-length human Nurr1 (Fig. 4a, b) which better reflects the physiological setting than the hybrid reporter gene assay (cf. Supplementary Fig. 2). Nurr1 can act as a monomer, homodimer, and RXR heterodimer on different response elements¹⁴. 36 robustly activated the Nurr1 homodimer (NurRE, EC₅₀ 0.094 μM; Fig. 4a) and the Nurr1-RXR heterodimer (DR5, EC₅₀ 0.165 μM; Fig. 4b) but interestingly was inactive on the Nurr1 monomer (NBRE; Fig. 4a) indicating an unprecedented Nurr1 dimer preference. The RXR agonist bexarotene caused generally reduced activity of DR5 (Supplementary Fig. 5) but enhanced the potency of 36 by a factor of >5 (EC₅₀ 0.032 μM (DR5 w. 0.1 μM BEX)) suggesting potentially cooperative binding⁴² to and activation of the Nurr1-RXR heterodimer.

36 exhibited high-affinity binding (K_d 0.17 μM) to the Nurr1 LBD in ITC (Fig. 4c) orthogonally validating its potent Nurr1 agonism. In astrocytes (T98G), 36 induced expression of the Nurr1-regulated genes tyrosine hydroxylase (TH), vesicular amino acid transporter 2 (VMAT2), and superoxide dismutase 2 (SOD2) at low concentrations (0.1 μM, 0.3 μM) supporting cellular target engagement (Fig. 4d). Selectivity profiling revealed a preference of 36 for Nurr1 over Nur77 (Table 6) and no activity outside the NR4A family at 3 μM corresponding to >30-fold selectivity (Fig. 4e). Moreover, 36 was non-toxic in N27 rat neurons, which can be used for neurodegeneration models^{46,43}, and in HEK293T cells at 10 μM which is two orders of magnitude above its EC₅₀ value (Fig. 4f). AQ, in contrast, exhibited considerable toxicity with only ~20% remaining N27 metabolic activity at a concentration (30 μM) that may be considered necessary for confident target engagement given its low potency. With its favorable profile fulfilling the highest quality criteria for chemical tools^{44,45}, 36 thus emerges as a next-generation tool to study the effects of Nurr1 modulation by AQ-type ligands.

To boost the value of 36 as a chemical tool, we aimed to complement it with a structurally matched negative control compound for which 29 appeared suitable. 29 strongly resembles 36 in its chemical structure and physicochemical characteristics but exhibited no Nurr1 agonism in a cellular setting at 10 μM and revealed no detectable binding to Nurr1 in ITC (Table 6). Further profiling of 29 revealed no effect on Nur77 and NOR-1, no activation of full-length Nurr1, and no induction of Nurr1-regulated gene expression (Fig. 4d). Thus, 29 is at least 100-fold less active than 36 as Nurr1 modulator and suitable as negative control.

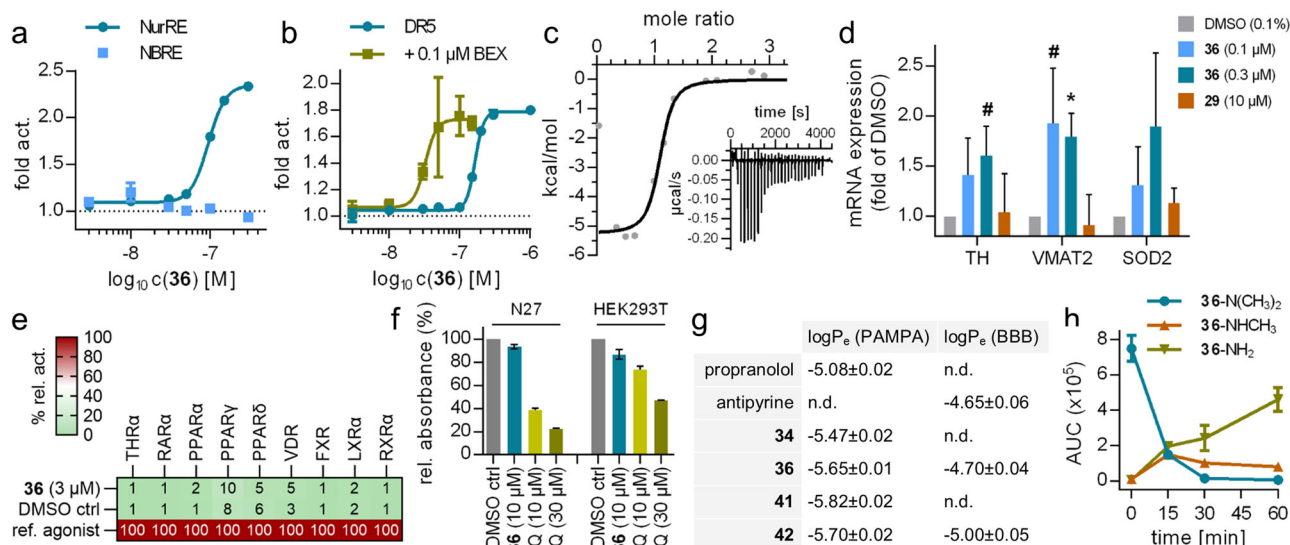


Fig. 4 | Orthogonal validation and profiling of 36. **a** Effects of 36 on the human full-length Nurr1 homodimer (NurRE) and monomer (NBRE). Data are the mean \pm S.E.M. fold activation vs. DMSO ctrl; $n \geq 3$. **b** Effects of 36 on the Nurr1-RXR heterodimer (DR5) in the absence and presence of bexarotene (0.1 μ M). Data are the mean \pm S.E.M. fold activation vs. DMSO ctrl or vs. 0.1 μ M BEX; $n \geq 3$. **c** Binding of 36 to the Nurr1 LBD (K_d 0.17 μ M, $n = 1.0$) determined by ITC. The fitting of the heat of binding is shown and the isotherm at 25 $^{\circ}$ C is shown as inset. **d** Effects of 36 and 29 on the expression of the Nurr1-regulated tyrosine hydroxylase (TH), vesicular amino acid transporter 2 (VMAT2), and superoxide dismutase 2 (SOD2) in astrocytes (T98G). Data are the mean \pm S.E.M. fold mRNA induction vs. DMSO ctrl;

$n = 3$; * $p < 0.1$, * $p < 0.05$ (t-test vs. DMSO ctrl). **e** Selectivity screening of 36 on nuclear receptors. Heatmap shows the mean relative activation compared to reference ligands (listed in the methods section); $n = 3$. **f** 36 (10 μ M) had no toxic effect in a WST-8 assay in N27 rat neurons and HEK293T cells. AQ (1, 10 and 30 μ M) was toxic. Data are the mean \pm S.E.M. rel. absorbance (450 nm); $n \geq 3$. **g** Permeability of Nurr1 agonists in a parallel artificial membrane permeability assay (PAMPA) and in a cellular model of the blood-brain-barrier (BBB). Propranolol and the brain-penetrant reference antipyryne for comparison. Data are the mean \pm SD; $n = 6$. **h** Metabolism of 36 by rat liver microsomes resulted in demethylation of the dimethylamino group. Data are the mean \pm SD; $n = 4$.

To further explore the potential of 36 as a chemical tool for in vivo applications, we evaluated its pharmacokinetic parameters. 36 exhibited favorable permeability in a parallel artificial membrane permeability assay (PAMPA) and a cellular model of the blood-brain barrier using the human brain endothelial cell-line HBEC-5i on trans-well plates⁴⁶ (Fig. 4g) as indicators of good absorption and brain penetration. The stability of 36 against degradation by rat liver microsomes was low, however, pointing to limited metabolic stability (Fig. 4h). Closer inspection suggested that 36 was almost exclusively degraded by demethylation of the dimethylamino motif. The initially formed monomethylamine (35) retained slightly reduced Nurr1 agonism (Table 5) while the eventually dominant fully demethylated amine 38 was less active (Table 7). We aimed to overcome the metabolic liability of 36 and obtain an analogue suitable for in vivo applications and hence probed replacement of the labile motif (Table 7). The introduction of cyclic amino substituents (39, 40) was not productive as Nurr1 agonism was lost with these bulkier residues. Therefore, we moved our attention to the methoxy analogue 34, which exhibited similar Nurr1 agonist potency as the labile dimethylamine 36 and threefold higher stability against microsomal degradation. Extension of the methoxy group of 34 to an isopropoxy (41) or cyclopropoxy (42) motif was well tolerated in terms of Nurr1 agonism and significantly improved metabolic stability while mostly retaining membrane and BBB permeability (Fig. 4g). These results, therefore, demonstrate that the pharmacokinetic profile of the new Nurr1 agonist scaffold can be tuned to obtain candidates for in vivo application.

The Nurr1 agonist 36 rescued tyrosine hydroxylase expression in LRRK2 mutant midbrain organoids

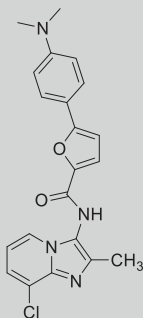
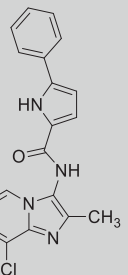
To evaluate the biological effects of the new Nurr1 agonist scaffold in a more (patho-)physiological setting and capture its full potential as a chemical tool and lead, we employed a PD model in a three-dimensional organoid system⁴⁷ derived from induced pluripotent stem cells (iPSC). Human midbrain organoids were generated from wildtype iPSC (isogenic control) and from iPSC bearing a G2019S mutation in the leucine-rich repeat kinase 2 (LRRK2) gene. LRRK2 mutation is among the most common genetic

causes of PD⁴⁸ and the G2019S mutation enhancing the kinase activity of LRRK2 has been correlated with increased α -synuclein accumulation, mitochondrial dysfunction, impaired dopamine signaling, and ultimately progressive dopamine neuron loss in the human brain^{48,49}. Using this in vitro disease model, we evaluated the impact of 36 and 29 on the dopamine neuron marker TH in 44 days old organoids (Fig. 5). Compared to the isogenic control, LRRK2 mutant organoids exhibited significantly diminished Nurr1 and TH mRNA expression (Fig. 5a, b). Treatment with the Nurr1 agonist 36 rescued the TH levels in LRRK2 mutant organoids as evident in mRNA transcript level (Fig. 5c) and histologically by staining for TH (Fig. 5b, d). TH transcript levels of mutant organoids further supporting the therapeutic potential of Nurr1 activation in PD. A weaker efficacy of 36 on TH levels in wild-type organoids may indicate that Nurr1 activity in these organoids was sufficient and that therapeutic Nurr1 activation may unfold stronger when Nurr1 activity is pathologically diminished. Importantly, Nurr1 levels were not altered by treatment with 36 (Fig. 5e) underscoring that its effects on TH expression were mediated by direct Nurr1 activation. Compound 29 did not affect TH and Nurr1 levels in organoids supporting its suitability as negative control.

Conclusion

Nurr1 is attracting remarkable interest as a candidate target for neurodegenerative disease treatment¹². However, the therapeutic potential of the nuclear receptor is mainly supported by knockout studies and observations from patients¹², and target validation with high-quality chemical tools is pending. AQ was discovered as a direct Nurr1 modulator and used in several pharmacological studies^{24,25} but is only a weak Nurr1 agonist and exhibits unspecific effects¹⁹ disqualifying the antimalarial as a chemical tool. Despite recent progress with an optimized Nurr1 agonist providing further evidence for the therapeutic value of Nurr1 activation in PD models³⁶, the promising effects observed with AQ require validation. Here, we have developed potent Nurr1 agonists from AQ with extensively validated activity and lacking the structural elements of AQ mediating unspecific toxicity to enable robust

Table 6 | Characterization of NR4A agonist 36 and negative control 29 demonstrating high chemical tool quality^{44,45}

		
	36	29
EC ₅₀ (Nurr1)	0.090 ± 0.005 μM	no activation (10 μM)
EC ₅₀ (Nur77)	0.33 ± 0.04 μM	no activation (10 μM)
EC ₅₀ (NOR-1)	0.11 ± 0.03 μM	no activation (10 μM)
EC ₅₀ (NBRE)	no activation (1 μM)	no activation (10 μM)
EC ₅₀ (NurRE)	0.094 ± 0.003 μM	no activation (10 μM)
EC ₅₀ (DR5) [+0.1 μM BEX]	0.165 ± 0.004 μM [0.032 ± 0.007 μM]	no activation (10 μM)
K _d (Nurr1 LBD)	0.17 μM	no binding ^b
NR selectivity ^c	inactive (3 μM)	n.d.
toxicity ^d	inactive (10 μM)	inactive (10 μM)
aq. solubility	6.8 mg/L	4.1 mg/L
SlogP ^e	4.87	4.54

^aNurr1 modulation was determined in a Gal4-Nurr1 hybrid reporter gene assay. Max. activation refers to the maximum effect vs. 0.1% DMSO control. Data are the mean ± SD; *n* ≥ 3. ^bNo binding observable in ITC with 100 μM **29** and 30 μM protein (Supplementary Fig. 6). ^cNuclear receptor selectivity was determined in Gal4-hybrid reporter gene assays for THRα, RARα, PPARα/γ/δ, VDR, FXR, LXRα and RXRα (Fig. 4e). ^dCytotoxicity was evaluated in N27 (**36**) and HEK293T (**29**, **36**) cells using a WST-8 assay (Fig. 4f). ^eSlogP was computed with RDKit⁶³ software.

biological studies on Nurr1 modulation with AQ-derived agonists. Scaffold-hopping, fragment optimization, and replacement of unfavorable motifs generated potent Nurr1 agonists with preferable chemical features and experimentally confirmed high-affinity binding to the Nurr1 LBD. **36** and the structurally matched negative control **29** fulfil the highest quality criteria⁴⁴ as a next-generation chemical tool for biological studies on Nurr1 to advance Nurr1 modulation as a therapeutic strategy in neurodegeneration and beyond.

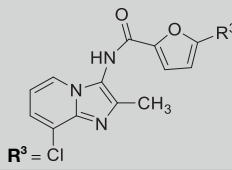
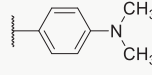
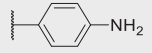
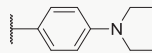
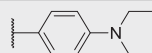
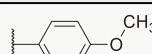

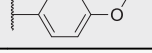
Chemistry

Compounds **7**, **8**, **12** and **14-24** were prepared by Groebke-Blackburn reaction according to Fig. 6. 3-Chloropyridine-2-amine (**43**) and 4-chloropyridine-2-amine (**44**) were cyclized with the aldehydes **45-57** and 1,1,3,3-tetramethylbutylisocyanide followed by acid-mediated cleavage to **7**, **8** and **14-24** using 4 N HCl in dioxane or TFA/CH₂Cl₂ (1:1). 1,1,3,3-Tetramethylbutylisocyanide (**63**) was commercially available. 3-Amino-8-chloroimidazo[1,2-*a*]pyridine (**12**) was prepared by nitration of 8-chloroimidazo[1,2-*a*]pyridine (**64**) followed by reduction with iron.

Compounds **26-36** were obtained by amide coupling of 3-amino-8-chloro-2-methylimidazo[1,2-*a*]pyridine (**8**) and the carboxylic acids **72-81** using HATU or thionyl chloride (Fig. 7). The carboxylic acids **72** and **73** were prepared by Suzuki coupling of aryl bromide **67** with the boronates **68**, **69** to **70**, **71** followed by alkaline ester hydrolysis. **74-81** were commercially available.

The fused derivative **37** was obtained from **24** via amide coupling with 5-bromofuran-2-carbonyl chloride (**82**) and subsequent Suzuki-Miyaura reaction with **73** according to Fig. 8. Similarly, **38-42** were synthesized from 3-amino-8-chloro-2-methylimidazo[1,2-*a*]pyridine (**8**) by amide coupling with 5-bromofuran-2-carboxylic acid (**81**) to **84** and Suzuki-Miyaura coupling with the boronates **85-89** (Fig. 9).

Table 7 | Optimization of 36 for microsomal stability

ID		EC ₅₀ (Nurr1) (max. act.) ^a	microsomal half-life ^b
	R ³ = Cl		
36		0.090 ± 0.005 μM (2.1 ± 0.1-fold)	6.3 ± 0.3 min.
38		<1.2-fold activation	n.d.
39		inactive (10 μM ^c)	n.d.
40		inactive (10 μM ^c)	n.d.
34		0.16 ± 0.06 μM (1.7 ± 0.1-fold)	18 ± 2 min.
41		0.12 ± 0.03 μM (2.1 ± 0.2-fold)	42 ± 5 min.
42		0.12 ± 0.06 μM (1.5 ± 0.2-fold)	78 ± 7 min.

^aNurr1 modulation was determined in a Gal4-Nurr1 hybrid reporter gene assay. Max. activation refers to the maximum effect vs. 0.1% DMSO control. Data are the mean ± SD; *n* ≥ 3. ^bStability against degradation by rat liver microsomes was determined by LCMS. n.d. - not determined.

^cHighest non-toxic concentration.

Experimental procedures

Chemistry

General. All chemicals were of reagent grade, purchased from commercial sources (e.g., Sigma-Aldrich, TCI, BLDpharm), and used without further purification unless otherwise specified. All reactions were conducted under a nitrogen or argon atmosphere and in absolute solvents purchased from Sigma-Aldrich. Other solvents, especially for work-up procedures, were of reagent grade or purified by distillation (*iso*-hexane, cyclohexane, ethyl acetate, EtOH). Reactions were monitored by thin layer chromatography (TLC) on TLC Silica gel 60 F254 coated aluminum sheets by Merck and visualized under ultraviolet light (254 nm) or by using ninhydrin or Ehrlich's reagent stains. Purification by column chromatography was performed on a puriFlash® XS520Plus system (Advion, Ithaca, NY, USA) using high-performance spherical silica columns (SIHP, 50 μm) by Interchim and a gradient of *iso*-hexane or cyclohexane to ethyl acetate. Reversed-phase column chromatography was performed on a puriFlash® 5.250 system (Advion) using C18HP columns (SIHP, 15 μm) by Interchim and a gradient of H₂O with 10% MeCN to 100% MeCN (HPLC gradient grade). Mass spectra were obtained on a puriFlash®-CMS system (Advion) using atmospheric pressure chemical ionization (APCI). HRMS were obtained with a Thermo Finnigan LTQ FT instrument for electron impact ionization (EI) or electrospray ionization (ESI). NMR spectra were recorded on Bruker Avance III HD 400 MHz or 500 MHz spectrometers equipped with a CryoProbe™ Prodigy broadband probe (Bruker). Chemical shifts are reported in δ values (ppm) relative to residual protium signals in the NMR solvent (¹H-NMR: acetone-*d*₆: δ = 2.04 ppm; DMSO-*d*₆: δ = 2.50 ppm; MeOD-*d*₄: δ = 3.31 ppm, ¹³C-NMR: acetone-*d*₆: δ = 206.26, 29.84 ppm; DMSO-*d*₆: δ = 39.52 ppm; MeOD-*d*₄: δ = 49.0 ppm), coupling constants (*J*) in hertz (Hz). The purity of the compounds was determined by ¹H NMR (qHNMR) according to the method described by Pauli et al.⁵⁰ with internal calibration. To ensure accurate determination of peak area

Fig. 5 | Treatment of midbrain organoids with the Nurr1 agonist 36 increased the number of TH positive cells. **a** Midbrain organoids generated from human iPSC bearing a gain-of-function LRRK2 mutation (G2019S) displayed diminished Nurr1 and TH transcript levels compared to isogenic controls after 45 days. **b** Midbrain organoid sections stained for TH expressing cells by immunofluorescence. Scale bars represent 100 μm . **c** The Nurr1 agonist 36 but not the negative control 29 induced TH mRNA expression in LRRK2 mutant organoids and tended to enhance TH mRNA expression in isogenic controls. **d** The Nurr1 agonist 36 but not the negative control 29 enhanced the number of TH positive cells in LRRK2 mutant organoids and in isogenic controls. **e** Compound treatment did not affect Nurr1 levels. All data are the mean \pm SD; $n = 3$. * $p < 0.05$, ** $p < 0.01$ (unpaired, two-tailed Student's t -test).

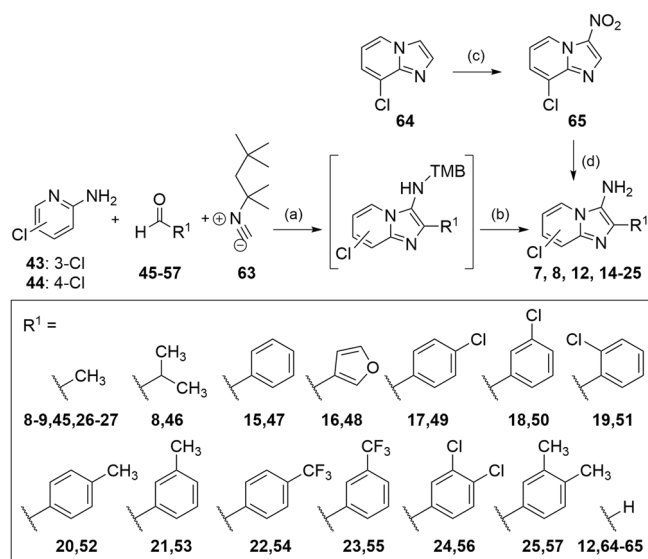
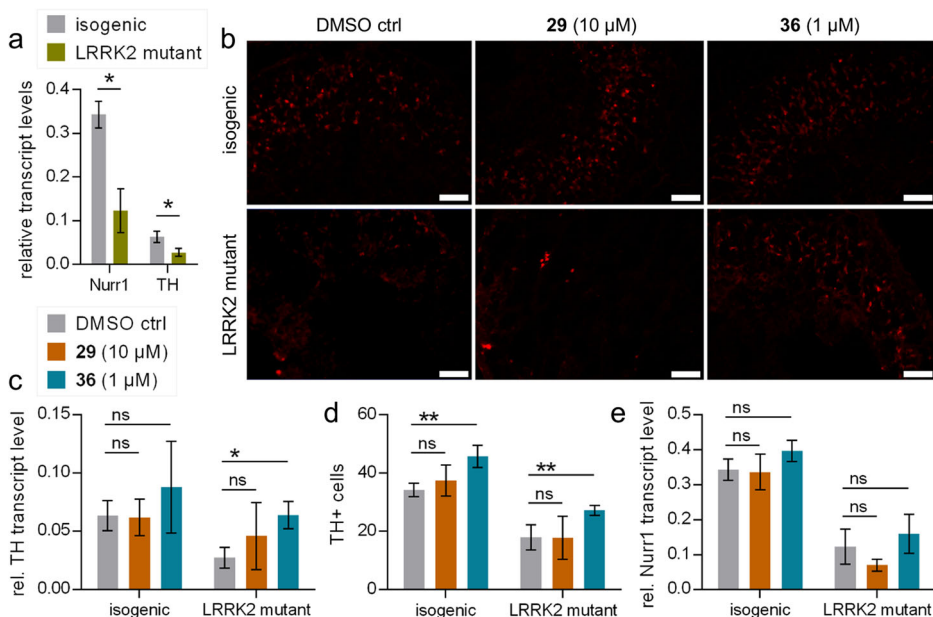


Fig. 6 | Synthesis of 7, 8, 12, 14-24, 26 and 27. Reagents & Conditions: **a** AcOH, MeOH, rt, 24–48 h; **b** TFA/DCM, rt, 30 min to overnight, 3–30% over two steps; **c** nitric acid, sulfuric acid, 0 $^{\circ}\text{C}$ – rt, 1 h, 93%; **d** iron, ammonium chloride, MeOH/water, reflux, overnight, 57%.

ratio, the qHNMR measurements were conducted under conditions allowing for complete relaxation. Ethyl 4-(dimethylamino)benzoate (LOT#BCCB6657, purity 99.63%), dimethyl terephthalate (LOT#BCBT9974, purity 99.95%) and maleic acid (LOT#BCBM8127V, purity 99.94%) were used as internal standards in MeOD- d_4 , DMSO- d_6 , or acetone- d_6 . All compounds for biological testing had a purity >95% according to quantitative ^1H NMR (qHNMR).

General procedure A for Groebke-Blackburn-Bienaymé reaction and hydrolysis. 2-Amino-3-chloropyridine (**43**, 1.0 eq.) or 2-amino-4-chloropyridine (**44**, 1.0 eq.), the respective aldehyde (**45–57**, 1.0–1.1 eq.) and glacial acetic acid (1.5 eq.) were dissolved in dry methanol (0.7 M) under nitrogen atmosphere. The mixture was stirred for 30–45 min. at room temperature (rt) for imine formation. 1,1,3,3-Tetramethylbutylisocyanid (**63**, 1.5 eq.) was subsequently added, and the

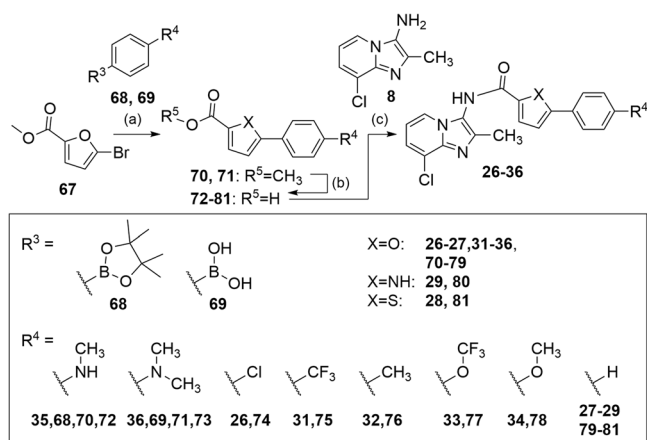


Fig. 7 | Synthesis of 26-36. Reagents & Conditions: **a** XPhos Pd G2, K_3PO_4 , water/dioxane, reflux, overnight, 86–97%; **b** LiOH, water/THF, rt, overnight, 67–73%; **c** HATU, DIPEA, DMF, rt, overnight, 33–100% or SOCl_2 , CHCl_3 reflux, 3 h, 11%.

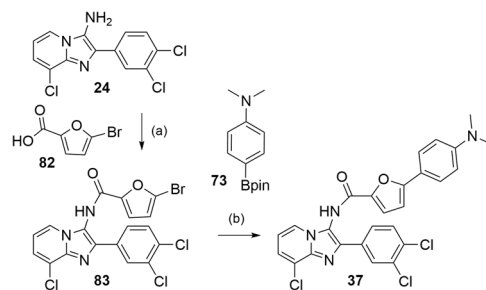


Fig. 8 | Synthesis of 37. Reagents & Conditions: **a** oxalyl chloride, pyridine, toluene, 0 $^{\circ}\text{C}$ – rt, 24 h, 64%; **b** tetrakis(triphenylphosphane)palladium(0), Na_2CO_3 , water/dioxane, reflux, overnight, 68%.

mixture was stirred at rt for 17–48 h. When TLC monitoring indicated completion, the isocyanide was quenched by the addition of 2N aqueous HCl (2 mL) and further stirring for 30 min. 2 N aqueous NaOH solution and ethyl acetate (10 mL) were then added, and the phases were separated. The aqueous layer was extracted with ethyl acetate (3x). The

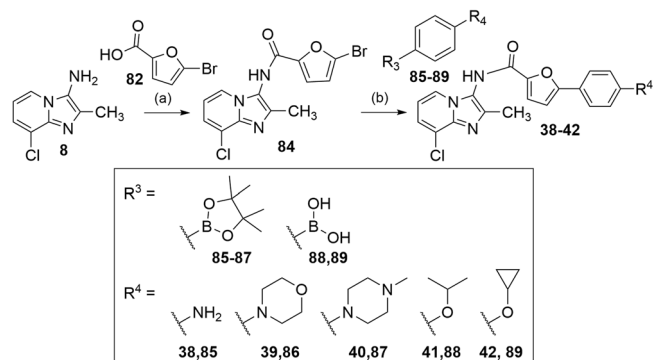


Fig. 9 | Synthesis of 38–42. Reagents & Conditions: **a** HATU, DIPEA, DMF, rt, overnight, 81%; **b** tetrakis(triphenylphosphane)palladium(0), Na₂CO₃, water/dioxane, reflux, overnight, 40–68%.

combined organic layers were dried over MgSO₄ and the solvent was evaporated under reduced pressure. The crude product was dissolved in a mixture of CH₂Cl₂ and trifluoroacetic acid (10 mL, 1:1) or 4 N HCl in dioxane (10 mL) and the mixture was stirred for 30–60 min. at rt. When TLC monitoring indicated completion, 2 N aqueous NaOH solution was added, phases were separated, and the aqueous layer was extracted with ethyl acetate (3x). The combined organic layers were dried over MgSO₄ and the solvents were evaporated under reduced pressure. The crude product was purified by flash column chromatography using a gradient of *iso*-hexane or cyclohexane/ethyl acetate as mobile phase, and potentially by reverse phase chromatography using a gradient of H₂O with 10% MeCN to 100% MeCN (HPLC gradient grade).

General procedure B for amide coupling with HATU. The respective carboxylic acid (**72–80**, 1.2 eq.) and 1-[bis(dimethylamino)methylene]-1*H*-1,2,3-triazolo[4,5-*b*]pyridinium 3-oxide hexafluorophosphate (HATU, 1.2 eq.) were dissolved in DMF (0.13 M). *N*-Ethyl-diisopropylamine (DIPEA, 0.13 M, 1.2 eq) was added and the mixture was stirred at rt for 40 min. 3-Aminoimidazo[1,2-*a*]pyridine (**8**, 1.0 eq.) was dissolved in DMF (0.11 M) and added to the activated carboxylic acid. The mixture was stirred at rt overnight. When TLC monitoring indicated completion, the solvent was removed under reduced pressure, the residue was dissolved in ethyl acetate and treated with 5% HCl (0.13 M). Phases were separated and the aqueous layer was extracted with ethyl acetate (3x). The combined organic layers were washed with 1 N aqueous NaOH solution and dried over MgSO₄. The solvent was evaporated under reduced pressure and the crude product was purified by flash column chromatography using a gradient of *iso*-hexane / ethyl acetate as mobile phase, and potentially by reverse phase chromatography using a gradient of H₂O with 10% MeCN to 100% MeCN (HPLC gradient grade).

8-Chloro-2-methylimidazo[1,2-*a*]pyridine-3-amine (8). Preparation according to general procedure A using 2-amino-3-chloropyridine (**43**, 821 mg, 6.39 mmol, 1.00 eq) and acetaldehyde (**45**, 39 μL, 7.03 mmol, 1.10 eq). **8** was obtained as a colorless solid (344 mg, 30%). ¹H-NMR (400 MHz, acetone-*d*₆): δ = 8.05 (dd, *J* = 6.8, 1.1 Hz, 1H), 7.11 (dd, *J* = 7.3, 1.0 Hz, 1H), 6.76 (t, *J* = 7.0 Hz, 1H), 4.17 (s, 2H), 2.33 (s, 3H). ¹³C-NMR (101 MHz, acetone-*d*₆): δ = 136.1, 130.1, 126.3, 121.5, 121.0, 119.8, 110.0, 11.9. MS (APCI+): *m/z* 181.9 ([M + H]⁺). HRMS (EI+): *m/z* calculated 181.0407 for C₈H₈ClN₃, found 181.0400 ([M + H]⁺). qHNMR (400 MHz, acetone-*d*₆, ethyl-4-(dimethylamino)benzoate as reference): purity = 97.5%.

8-Chloro-2-(3,4-dichlorophenyl)imidazo[1,2-*a*]pyridine-3-amine (24). Preparation according to general procedure A using 2-amino-4-chloropyridine (**43**, 1.29 g, 10.0 mmol, 1.00 eq) and 3,4-dichlorobenzaldehyde (**56**, 1.93 g, 11.0 mmol, 1.01 eq). **24** was obtained as a

yellow solid (197 mg, 6%). ¹H-NMR (400 MHz, acetone-*d*₆): δ = 8.41–8.35 (m, 1H), 8.30 – 8.23 (m, 1H), 8.20 – 8.12 (m, 1H), 7.630–7.56 (m, 1H), 7.27 (dd, *J* = 7.3, 1.1 Hz, 1H), 6.88 (t, *J* = 7.1 Hz, 1H), 4.83 (s, 2H). ¹³C-NMR (101 MHz, MeOD-*d*₄): δ = 137.2, 134.4, 132.1, 130.1, 130.0, 128.6, 128.0, 127.5, 126.3, 122.6, 121.7, 121.3, 111.3. MS (APCI+): *m/z* 311.9 ([M + H]⁺). HRMS (EI+): *m/z* calculated 310.9784 for C₁₃H₈Cl₃N₃, found 310.9778 ([M]⁺). qHNMR (400 MHz, acetone-*d*₆, ethyl-4-(dimethylamino)benzoate as reference) purity = 95.7%.

***N*-(8-Chloro-2-methylimidazo[1,2-*a*]pyridin-3-yl)-5-(4-(dimethylamino)phenyl)furan-2-carboxamide (36).** Preparation according to general procedure B using 8-chloro-2-methylimidazo[1,2-*a*]pyridine-3-amine (**8**, 50 mg, 0.28 mmol, 1.00 eq) and 5-(4-(dimethylamino)phenyl)furan-2-carboxylic acid (**73**, 76 mg, 0.33 mmol, 1.20 eq). **36** was obtained as a yellow solid (69 mg, 64%). ¹H-NMR (400 MHz, acetone-*d*₆): δ = 9.68 (s, 1H), 8.11 (d, *J* = 1.0 Hz, 1H), 7.77 (d, *J* = 8.5 Hz, 2H), 7.40 – 7.27 (m, 2H), 6.94 – 6.73 (m, 4H), 3.00 (s, 6H), 2.36 (s, 3H). ¹³C-NMR (101 MHz, acetone-*d*₆): δ = 157.7, 157.2, 151.0, 145.1, 139.1, 138.7, 125.9, 122.8, 122.6, 121.8, 118.0, 117.6, 117.0, 111.99, 111.0, 104.3, 39.4, 12.4. MS (APCI+): *m/z* 394.7 ([M + H]⁺). HRMS (EI+): *m/z* calculated 394.1197 for C₂₁H₁₉ClN₄O₂, found 394.1194 ([M]⁺). qHNMR (400 MHz, acetone-*d*₆, maleic acid as reference) purity = 95.1%.

***N*-(8-Chloro-2-methylimidazo[1,2-*a*]pyridin-3-yl)-5-phenyl-1*H*-pyrrole-2-carboxamide (29).** 5-Phenyl-1*H*-pyrrole-2-carboxylic acid (**80**, 74.0 mg, 396 μmol, 1.20 eq) was refluxed in thionyl chloride (4 mL) for 3 h. After cooling to rt, remaining thionyl chloride was removed under reduced pressure. 8-Chloro-2-methylimidazo[1,2-*a*]pyridine-3-amine (**8**, 60.0 mg, 330 μmol, 1.00 eq) dissolved in chloroform (5 mL) was added to the crude acyl chloride at 0 °C and the mixture was stirred at rt overnight. The solvent was removed under reduced pressure, the residue was dissolved in ethyl acetate and treated with 5% HCl (5 mL). Phases were separated, the aqueous layer was extracted with ethyl acetate (3x), and the combined organic layers were washed with 1 N aqueous NaOH solution and dried over MgSO₄. The solvent was removed under reduced pressure and the crude product was purified by flash column chromatography and reverse column chromatography giving compound **29** as a colorless solid (13 mg, 11%). ¹H-NMR (400 MHz, acetone-*d*₆): δ = 11.85 (s, 1H), 10.51 (s, 1H), 8.31 (d, *J* = 6.7 Hz, 1H), 7.98 (d, *J* = 7.5 Hz, 2H), 7.63 (d, *J* = 7.4 Hz, 1H), 7.41 (t, *J* = 7.7 Hz, 2H), 7.34–7.23 (m, 1H), 7.21–7.06 (m, 2H), 6.75–6.63 (m, 1H), 2.44 (s, 3H). ¹³C-NMR (101 MHz, acetone-*d*₆): δ = 159.6, 154.3, 154.1, 137.4, 136.7, 131.9, 128.7, 127.2, 126.2, 126.0, 125.0, 123.7, 118.9, 114.9, 113.1, 107.3, 11.2. qHNMR (400 MHz, acetone-*d*₆, dimethyl terephthalate as reference): purity = 97.1%. MS (APCI+): *m/z* 350.3 ([M]⁺). HRMS (ESI+): *m/z* calculated 351.0007 for C₁₉H₁₆ClN₄O⁺, found 351.10048 ([M + H]⁺).

***N*-(8-Chloro-2-(3,4-dichlorophenyl)imidazo[1,2-*a*]pyridin-3-yl)-5-(4-(dimethylamino)phenyl)furan-2-carboxamide (37).** *N,N*-Dimethyl-4-(4,4,5,5-tetramethyl-1,3,2-dioxaborolan-2-yl)aniline (**69**, 40.8 mg, 0.165 mmol, 1.00 eq), 5-bromo-*N*-(8-chloro-2-(3,4-dichlorophenyl)imidazo[1,2-*a*]pyridin-3-yl)furan-2-carboxamide (**84**, 80.0 mg, 0.165 mmol, 1.00 eq) and sodium carbonate (52.5 mg, 3.00 mol, 3.00 eq) were dissolved in dioxane/H₂O (10 mL, 9:1). The solution was degassed by freeze-pump-thaw cycles (3x). Pd(PPh₃)₄ (9.53 mg, 8.25 μmol, 0.05 eq) was added and the mixture was refluxed for 3 h under argon atmosphere. The resulting suspension was filtered, and the precipitate was washed with 2 N aqueous NaOH solution, EtOH, methylene chloride, and brine giving **37** as a colorless solid (59 mg, 68%). ¹H-NMR (400 MHz, DMSO-*d*₆): δ = 10.86 (s, 1H), 8.27–8.17 (m, 2H), 8.02–7.94 (m, 1H), 7.85–7.72 (m, 3H), 7.60 (d, *J* = 7.3 Hz, 1H), 7.57–7.50 (m, 1H), 7.02–6.92 (m, 2H), 6.80 (d, *J* = 8.8 Hz, 2H), 2.98 (s, 6H). ¹³C-NMR (126 MHz, DMSO-*d*₆): δ = 158.0, 151.1, 144.5, 139.7, 136.5, 136.0, 134.1, 132.0, 131.6, 128.6, 127.1, 126.4, 125.6, 124.1, 122.0, 119.4, 117.3, 115.3, 113.0, 112.4, 110.4, 105.2, 31.2. qHNMR (400 MHz, DMSO-*d*₆, maleic

acid as reference): purity = 96.1%. MS (APCI+): m/z 524.2 ($[M + H]^+$). HRMS (ESI+): m/z calculated 525.0646 for $C_{26}H_{20}Cl_3N_4O_2^+$, found 525.0641 ($[M + H]^+$).

N-(8-Chloro-2-methylimidazo[1,2-*a*]pyridin-3-yl)-5-(4-cyclopropoxyphenyl)furan-2-carboxamide (42). 4-Cyclopropoxyphenylboronic acid (**89**, 30.1 mg, 169 μ mol, 1.00 eq), 5-bromo-*N*-(8-chloro-2-methylimidazo[1,2-*a*]pyridin-3-yl)furan-2-carboxamide (**84**, 60.0 mg, 0.169 mmol, 1.00 eq) and sodium carbonate (53.7 mg, 3.00 mol, 3.00 eq) were dissolved in dioxane/ H₂O (10 mL, 9:1). The solution was degassed by freeze-pump-thaw cycles (3x). Pd(PPh₃)₄ (9.76 mg, 8.45 μ mol, 0.05 eq) was added and the mixture was refluxed for 3 h under argon atmosphere. The resulting suspension was filtered through Celite and the solvent was removed under reduced pressure. The residue was dissolved in 2 N aqueous NaOH solution and was extracted with ethyl acetate (3x). The combined organic layers were dried over MgSO₄ and the solvent was removed under reduced pressure. The crude product was purified by flash column chromatography and reverse column chromatography giving **42** as a colorless solid (45 mg, 65%). ¹H-NMR (400 MHz, acetone-*d*₆): δ = 9.76 (s, 1H), 8.13 (d, J = 1.0 Hz, 1H), 7.89 (d, J = 8.5 Hz, 2H), 7.41–7.29 (m, 2H), 7.22–7.09 (m, 2H), 6.98 (d, J = 3.6 Hz, 1H), 6.88 (t, J = 6.8 Hz, 1H), 3.93–3.85 (m, 1H), 2.36 (s, 3H), 0.89–0.67 (m, 4H). ¹³C-NMR (126 MHz, acetone-*d*₆): δ = 159.8, 157.1, 156.5, 145.9, 139.1, 138.7, 126.1, 122.9, 122.8, 122.6, 121.9, 117.8, 116.9, 115.4, 111.0, 106.0, 50.8, 12.4, 5.7. qHNMR (400 MHz, acetone-*d*₆, ethyl-4-(dimethylamino)benzoate as reference): purity = 97.5%. MS (APCI+): m/z 407.7 ($[M + H]^+$). HRMS (ESI+): m/z calculated 408.1109 for $C_{22}H_{19}ClN_3O_3^+$, found 408.1103 ($[M + H]^+$).

5-Bromo-*N*-(8-chloro-2-(3,4-dichlorophenyl)imidazo[1,2-*a*]pyridin-3-yl)furan-2-carboxamide (83). 5-Bromofuran-2-carboxylic acid (**82**, 345 mg, 1.81 mmol, 3.14 eq) was dissolved in methylene chloride (2 mL) under Ar atmosphere. Oxalyl chloride (310 μ L, 3.62 mmol, 6.3 eq) was added dropwise to the solution at 0 °C. After 3 h the solvent was removed under reduced pressure and 8-chloro-2-(3,4-dichlorophenyl)imidazo[1,2-*a*]pyridine-3-amine (**24**, 180 mg, 576 μ mol, 1.00 eq) dissolved in a mixture of pyridine (1 mL) and toluene (4 mL) was added and the mixture was stirred at rt overnight. 2 N aqueous NaOH solution (10 mL) was added, phases were separated, and the aqueous layer was extracted with ethyl acetate (3x). The combined organic layers were dried over MgSO₄ and the solvent was removed under reduced pressure. The crude product was purified by flash column chromatography using a gradient of cyclohexane/ ethyl acetate as mobile phase giving **83** as a brown solid (180 mg, 64%). ¹H-NMR (400 MHz, DMSO-*d*₆): δ = 10.87 (s, 1H), 8.29–8.24 (m, 1H), 8.15 (d, J = 2.0 Hz, 1H), 7.92 (dd, J = 8.4, 2.1 Hz, 1H), 7.76 (d, J = 8.4 Hz, 1H), 7.62–7.57 (m, 1H), 7.50 (d, J = 3.6 Hz, 1H), 7.02–6.92 (m, 2H). ¹³C-NMR (101 MHz, DMSO-*d*₆): δ = 157.0, 148.8, 139.8, 136.5, 133.9, 132.0, 131.7, 131.1, 128.6, 127.1, 127.1, 125.7, 124.1, 122.0, 119.2, 117.2, 115.2, 113.1. MS (APCI+): m/z 483.3 ($[M + H]^+$).

5-Bromo-*N*-(8-chloro-2-methylimidazo[1,2-*a*]pyridin-3-yl)furan-2-carboxamide (84). Preparation according to general procedure B using 8-chloro-2-methylimidazo[1,2-*a*]pyridine-3-amine (**8**, 340 mg, 1.87 mmol, 1.00 eq) and 5-bromofuran-2-carboxylic acid (**82**, 429 mg, 2.24 mmol, 1.20 eq) yielded compound **84** as a colorless solid (536 mg, 81%). ¹H-NMR (400 MHz, MeOD-*d*₄): δ = 8.00 (d, J = 1.0 Hz, 1H), 7.43 (d, J = 1.0 Hz, 1H), 7.33 (d, J = 3.6 Hz, 1H), 6.91 (t, J = 7.1 Hz, 1H), 6.73 (d, J = 3.7 Hz, 1H), 2.39 (s, 3H). ¹³C-NMR (101 MHz, MeOD-*d*₄): δ = 157.5, 148.5, 139.5, 138.1, 126.6, 124.2, 122.2, 121.4, 118.5, 116.3, 114.4, 111.9, 11.2. MS (APCI+): m/z 355.4 ($[M + H]^+$).

Synthetic procedures and analytical data for **8-9**, **12**, **14-42** are provided as Supplementary Methods in the Supplementary Information (pdf). NMR spectra (¹H, ¹³C and qH) and HRMS of **8-9**, **12**, **14-42** are provided in Supplementary Data 1.

In vitro Characterization

Hybrid reporter gene assays. Nurr1 modulation was determined in a Gal4 hybrid reporter gene assay in HEK293T cells (German Collection of Microorganisms and Cell Culture GmbH, DSMZ) using pFR-Luc (Stratagene, La Jolla, CA, USA; reporter), pRL-SV40 (Promega, Madison, WI, USA; internal control) and pFA-CMV-hNurr1-LBD¹⁴, coding for the hinge region and ligand binding domain of the canonical isoform of human Nurr1. Cells were cultured in Dulbecco's modified Eagle's medium (DMEM), high glucose supplemented with 10% fetal calf serum (FCS), sodium pyruvate (1 mM), penicillin (100 U/mL), and streptomycin (100 μ g/mL) at 37 °C and 5% CO₂ and seeded in 96-well plates (3×10^4 cells/well). After 24 h, the medium was changed to Opti-MEM without supplements, and cells were transiently transfected using Lipofectamine LTX reagent (Invitrogen, Carlsbad, CA, USA) according to the manufacturer's protocol. Five hours after transfection, cells were incubated with the test compounds in Opti-MEM supplemented with penicillin (100 U/mL), streptomycin (100 μ g/mL), and 0.1% DMSO for 16 h before luciferase activity was measured using the Dual-Glo Luciferase Assay System (Promega) according to the manufacturer's protocol on a Tecan Spark luminometer (Tecan Deutschland GmbH, Crailsheim, Germany). Firefly luminescence was divided by Renilla luminescence and multiplied by 1000 resulting in relative light units (RLU) to normalize for transfection efficiency and cell growth. Fold activation was obtained by dividing the mean RLU of the test compound by the mean RLU of the untreated control. All samples were tested in at least three biologically independent experiments in duplicates. For dose-response curve fitting and calculation of EC₅₀ values, the equation "[Agonist] vs. response -- Variable slope (four parameters)" was used in GraphPad Prism (version 7.00, GraphPad Software, La Jolla, CA, USA). Selectivity profiling was performed with identical procedures using pFA-CMV-Nur77-LBD¹⁴, pFA-CMV-NOR-1-LBD¹⁴, pFA-CMV-THRA-LBD⁵¹, pFA-CMV-RAR α -LBD⁵², pFA-CMV-PPAR α -LBD⁵³, pFA-CMV-PPAR γ -LBD⁵³, pFA-CMV-PPAR δ -LBD⁵³, pFA-CMV-LXR α -LBD⁵⁴, pFA-CMV-FXR-LBD⁵⁵ and pFA-CMV-hRXR α -LBD⁵⁶.

Full-length Nurr1 reporter gene assays. Activation of full-length human Nurr1 was studied in transiently transfected HEK293T cells using the reporter plasmids pFR-Luc-NBRE¹⁴, pFR-Luc-POMC¹⁴ or pFR-Luc-DR5¹⁴ each containing one copy of the respective human Nurr1 response element NBRE N13, NurRE, or DR5. The full-length human nuclear receptor Nurr1 (pcDNA3.1-hNurr1-NE; Addgene plasmid #102363) and, for DR5, RXR α (pSG5-hRXR)⁵⁷ were overexpressed. pRL-SV40 (Promega) was used for the normalization of transfection efficacy and to observe test compound toxicity. Cells were cultured in Dulbecco's modified Eagle's medium (DMEM), high glucose supplemented with 10% fetal calf serum (FCS), sodium pyruvate (1 mM), penicillin (100 U/mL), and streptomycin (100 μ g/mL) at 37 °C and 5% CO₂ and seeded in 96-well plates (3×10^4 cells/well). After 24 h, the medium was changed to Opti-MEM without supplements, and cells were transiently transfected using Lipofectamine LTX reagent (Invitrogen) according to the manufacturer's protocol. Five hours after transfection, cells were incubated with the test compounds in Opti-MEM supplemented with penicillin (100 U/mL), streptomycin (100 μ g/mL) and 0.1% DMSO for 16 h before luciferase activity was measured using the Dual-Glo Luciferase Assay System (Promega) according to the manufacturer's protocol on a Tecan Spark luminometer (Tecan Deutschland GmbH). Firefly luminescence was divided by Renilla luminescence and multiplied by 1000 resulting in relative light units (RLU) to normalize for transfection efficiency and cell growth. Fold activation was obtained by dividing the mean RLU of the test compound by the mean RLU of the untreated control. All samples were tested in at least three biologically independent experiments in duplicates. For dose-response curve fitting and calculation of EC₅₀ values, the equation "[Agonist] vs. response -- Variable slope (four parameters)" was used in GraphPad Prism (version 7.00, GraphPad Software).

Isothermal Titration Calorimetry (ITC). ITC experiments were conducted on an Affinity ITC instrument (TA Instruments, New Castle, DE) at 25 °C with a stirring rate of 75 rpm. Nurr1 LBD protein (5–30 μM, expressed as described previously²¹) in buffer (20 mM Tris pH 7.5, 100 mM NaCl, 5% glycerol) containing 1–4% DMSO was titrated with the test compounds (30–150 μM in the same buffer containing 1–4% DMSO) in 26 injections (1 × 1 μL, 25 × 3–4 μL) with an injection interval of 120–150 s. As control experiments, the test compounds were titrated to the buffer, and the buffer was titrated to the Nurr1 LBD protein under otherwise identical conditions. Results were analyzed using NanoAnalyze software (version 3.11.0, TA Instruments, New Castle, DE) with independent binding models.

Evaluation of Nurr1-regulated VMAT2 expression in T98G cells.

T98G (ATCC, CRL-1690) were grown in DMEM, high glucose supplemented with 10% FCS, sodium pyruvate (1 mM), penicillin (100 U/mL), and streptomycin (100 μg/mL) at 37 °C and 5% CO₂ and seeded at a density of 250,000 cells per well in 12-well plates. After 24 h, medium was changed to DMEM, high glucose supplemented with 0.2% fetal calf serum (FCS), penicillin (100 U/mL), and streptomycin (100 μg/mL) and the cells were incubated for another 24 h before stimulation with the test compounds (**36** (0.3 μM), **29** (10 μM)) solubilized with 0.1% DMSO or with 0.1% DMSO as a negative control. After 16 h of incubation, the medium was removed, cells were washed with phosphate-buffered saline (PBS) and after full aspiration of residual liquids, they were immediately frozen at –80 °C until further processing. Total RNA was isolated using the E.Z.N.A.® Total RNA Kit I (Omega Bio-tek, Norcross, USA) following the manufacturer's instructions. RNA concentration and purity were assessed using a NanoDrop™ One UV/VIS spectrophotometer (Thermo Fisher Scientific, Waltham, USA) at 260/280 nm. Right before reverse transcription (RT), RNA was linearized at 65 °C for 10 min and then immediately incubated on ice for at least 1 min. Reverse transcription was performed using 2 μg total RNA, 20 U Recombinant RNasin® Ribonuclease Inhibitor (Promega, Mannheim, Germany), 100 U SuperScript® IV Reverse Transcriptase including 5x First Strand Buffer and 0.1 M dithiothreitol (Thermo Fisher Scientific, Waltham, USA), 3.75 ng linear acrylamide, 625 ng random hexamere primers (#11277081001, Merck, Darmstadt, Germany) and 11.25 nmol deoxynucleoside triphosphate mix (2.8 nmol each ATP, TTP, CTP, GTP; #R0186, Thermo Fisher Scientific, Waltham, USA) at a volume of 22.45 μL at 50 °C for 10 min and 80 °C for 10 min using a Thermal cycler XT⁹⁶ (VWR International, Darmstadt, Germany). Quantitative polymerase chain reaction (qPCR) was conducted using an Applied Biosystems™ QuantStudio 1 (Waltham, USA) and a SYBR green-based detection method. Appropriately diluted cDNA was added to 6 pmol of forward and reverse primer, respectively, 0.8 U Taq DNA Polymerase (#M0267, New England Biolabs, Ipswich, USA), 40 ppm SYBR® Green I (#S9430, Sigma Aldrich, St. Louis, USA), 15 nmol deoxynucleoside triphosphate mix (as indicated above), 60 nmol MgCl₂, 4 μg bovine serum albumin (#B14, Thermo Fisher Scientific, Waltham, USA), 20% BioStab PCR Optimizer II (#53833, Merck, Darmstadt, Germany), and 10% Taq buffer without detergents (#B55, Thermo Fisher Scientific, Waltham, USA) topped up at a final volume of 20 μL with ddH₂O. Samples underwent 40 cycles of 15 s denaturation at 95 °C, 15 s of primer annealing at 59.4 or 62.4 °C (depending on the primer), and 20 s of elongation at 68 °C. PCR product specificity was evaluated using a melting curve analysis ranging from 65 to 95 °C. VMAT2, TH and SOD2 mRNA expression was normalized to GAPDH mRNA expression per each sample using the ΔCt-method. The following primers for the human genes were used. hVMAT2 (SLC18A2): 5'-GCT ATG CCT TCC TGC TGA TTG C-3' (fw) and 5'-CCA AGG CGA TTC CCA TGA CGT T-3' (rev); hTH: 5'-GCT GAA CAA GTG TCA TCA CCT G-3' (fw) and 5'-CCT GTA CTG GAA GGC GAT CTC A-3' (rev); hSOD2: 5'-CCA AAG GGG AGT TGC TGG AA -3' (fw) and 5'-GAA ACC AAG CCA ACC CCA AC -3' (rev); hGAPDH: 5'-AGG TCG GAG TCA ACG GAT TT-3' (fw) and 5'-TTC CCG TTC TCA GCC TTG AC-3' (rev).

Determination of aqueous solubility. The aqueous solubility of **29** and **36** was assessed by mixing 1 mg of each test compound with an appropriate volume of water for a theoretical concentration of 4 mM to obtain an oversaturated mixture. The mixture was agitated in a VWR Thermal Shake lite (VWR International GmbH, Darmstadt, Germany) for 24 h at 600 rpm and a constant temperature of 25 °C. The supersaturated mixtures were subsequently centrifuged at 23,300 rpm for 15 min (25 °C). Part of the supernatant was taken off for quantification by UV absorbance at 312 nm with external calibration. The external calibration samples contained 1% DMSO and the test samples were spiked with DMSO to 1% concentration right before the measurement. Absorbance was measured with a Tecan Spark luminometer (Tecan Deutschland GmbH, Crailsheim, Germany). The solubility test was repeated in three independent experiments.

Cytotoxicity assays. HEK293T cells were cultured at 37 °C and 5% CO₂ in DMEM high-glucose supplemented with sodium pyruvate (1 mM), penicillin (100 U/mL), streptomycin (100 μg/mL), and 10% fetal calf serum (FCS) and seeded at a density of 10,000 cells in 96-well plates pre-coated with a 10 μg/mL collagen G solution (Merck KGaA, L7213) at 37 °C for 30 min. N27 rat dopaminergic neural cells (SCC048, Sigma-Aldrich, Darmstadt, Germany) were grown in RPMI 1640 (Gibco, Thermo Fisher Scientific, Waltham) supplemented with 10% FCS, penicillin (100 U/mL), and streptomycin (100 μg/mL) at 37 °C and 5% CO₂ and seeded at a density of 10,000 cells in 96-well plates. After 24 h, the cells were treated with the solubilized (0.1% DMSO) test compounds in Opti-MEM supplemented with penicillin (100 U/mL) and streptomycin (100 μg/mL) for HEK293T cells or in RPMI 1640 supplemented with penicillin (100 U/mL), streptomycin (100 μg/mL) and 0.2% FCS for N27 cells. Each sample was prepared in four biologically independent repeats. After incubation for 24 h, the medium was refreshed and 10% water-soluble tetrazolinium salt (Cell Counting Kit-8, MedChemExpress) was added to assess metabolic activity. After 4 h, absorbance was measured at 450 nm using a Tecan Spark Cyto instrument (Tecan).

Evaluation of microsomal stability. To determine microsomal stability, test compounds (10 μM) were incubated in 100 mM potassium phosphate buffer at pH 7.4 (total volume of 100 μL) containing 0.5 mg/mL male rat liver microsomes (Sprague-Dawley, no. M9066, Merck KGaA, Darmstadt) and 1 mM NADPH for 0, 15, 30, or 60 min. At the end of the incubation time, microsomal activity was terminated by the addition of 500 μL MeCN and subsequent centrifugation at 1700 g for 5 min. A reaction mixture containing heat-inactivated microsomes (95 °C, 10 min) was prepared as a control for each compound. 5 μL supernatant of each sample was analyzed and the remaining concentrations of the respective test compounds at each time point were determined by LC-MS/MS on an API-3200-QTrap (Sciex) with an Agilent Technologies 1100 series setup including a binary pump (G1311A), a degasser (G1322A), and a Shimadzu SIL 20 A HT autosampler under the control of Analyst 1.6 (Sciex). A XBridge BEH C18 (3.5 μm, 150 mm×3 mm, Waters, protected with a 0.5 μm frit) stationary phase was used in combination with a gradient method starting with 0.1% formic acid in water (A) and MeCN (B) as mobile phase (A:B = 80:20) for 6 min going to A: B = 50:50 after 8 min. 5 μL of supernatant diluted in mobile phase starting conditions was loaded onto the column, separated at a flow rate of 400 μL/min, and detected and quantified per Area of MRM (multiple reaction monitoring) with the following transitions: *m/z* 381.797/145.000 (**34**); *m/z* 395.125/158.200 (**36**); *m/z* 409.822/131.000 (**41**); *m/z* 407.838/171.100 (**42**).

Parallel artificial membrane permeability assay (PAMPA). Passive lipid membrane diffusion of test compounds was determined using Merck Millipore MultiScreen Filter Plates (0.45 μm pore diameter, hydrophobic PVDF). The filter inserts were coated with 1% L-α-phosphatidylcholine (Fluka Analytical) in *n*-dodecan. The test

compounds were then added to the donor compartment at a final concentration of 500 μM in a phosphate buffer pH 7.4 containing 5% DMSO with a total volume of 150 μL . The acceptor compartment was filled with 300 μL PBS containing 5% DMSO. Additionally, three equilibrium samples were prepared by directly adding the donor solution to the acceptor compartment for the calculation of log Pe values. The filter plates were incubated for 18 h before the test compound concentrations in the acceptor compartments and in the equilibrium, samples were determined by UV absorbance at 320 nm (34), 360 nm (36), 310 nm (41), or 315 nm (42) with external calibration in a 96 well quartz plate on a SpectraMax M2e microplate reader (Molecular Devices). logPe values were calculated according to the formula published by Sugano and colleagues⁵⁸.

In vitro blood-brain-barrier model. Permeation of test compounds through a human brain endothelial cell barrier was evaluated using the Corning Costar 3470 Transwell Plate system (0.4 μm pore diameter with 6.5 mm inserts) and HBEC-5i cells (ATCC, CRL-3245). Filter inserts were coated one day before seeding with 50 μL 0.01% rat-tail collagen type I (C7661, Sigma-Aldrich) in PBS. 60,000 HBEC-5i cells in 100 μL HBEC-5i-Medium (DMEM/F12 with 10% FCS and 40 $\mu\text{g}/\text{mL}$ ECGS) were seeded after aspiration of the coating-supernatant in each insert with 600 μL HBEC-5i-Medium in each receiver well. After 24 h incubation at 37 °C with 5% CO_2 , the medium was exchanged to 600 μL T98G cell supernatant in receiver wells and 100 μL fresh HBEC-5i-Medium in inserts. The medium exchange was repeated every second day. On day 7 after seeding, the medium in the receiver wells was replaced by 600 μL Hank's balanced salt solution (HBSS) containing 10 mM HEPES and 0.1% DMSO and 100 μL test compound mixtures (antipyrine and test compound; each at 10 μM) in HBSS containing 10 mM HEPES and 0.1% DMSO were added to inserts. After 60 min incubation, 100 μL samples were taken from the receiver wells and diluted in 400 μL (75%/25% A/B; A=Formic acid 0.1% in water; B = Acetonitrile). Test compound concentrations in the samples were determined by LC-MS/MS on an API-3200-QTrap (Sciex) equipped with an Agilent Technologies 1100 series setup including a binary pump (G1311A), a degasser (G1322A), and a Shimadzu SIL 20 A HT autosampler under the control of Analyst 1.6 (Sciex). An XBridge BEH C18 (3.5 μm , 150 mm \times 3 mm, Waters, protected with a 0.5 μm frit) served as stationary phase in combination with a gradient method starting with 0.1% formic acid in water (A) and MeCN (B) as mobile phase (80%:20% = A: B) for 6 min going to (50%:50%) after 8 min. 5 μL of aspirated supernatant diluted in mobile phase starting conditions was loaded onto the column, separated at a flow rate of 400 $\mu\text{L}/\text{min}$, and quantified per Area of MRM (multiple reaction monitoring).

Organoid PD model. Cell lines: Human induced pluripotent stem cells (hiPSCs; iPSC-LRRK2 isogenic control and iPSC-LRRK2-G2019S) were cultured in Essential 8TM Flex Medium-Kit (Thermo Fisher) on vitronectin (VTN-N; Thermo Fisher) coated cell culture dishes. The cells were passaged every three days as clumps with 0.5 M EDTA (0.5 M EDTA, 5 M NaCl, PBS). The hiPSCs contained a NURR1 GFP reporter cassette and a single point mutation (G2019S) was incorporated into the LRRK2 gene, resulting in the generation of the PD iPSC-LRRK2-G2019S cell line⁴⁷ (cell lines were kindly provided by the Tchiew Lab, Cincinnati). Cells were regularly tested for pluripotency levels using the markers Nanog and Oct-4 and for mycoplasma contamination. Generation of human midbrain-like organoids: Human midbrain-like organoids (hMLOs) were formed according to the protocol of Jo et al.⁵⁹ In brief, hiPSCs were dissociated via accutase for 1 h at 37 °C into single cells after reaching 70% confluency. Subsequently, 10,000 cells were seeded in each well of a 96-well v-shaped ultra-low attachment plate (Sbio®) in neuronal induction media (NIC; DMEM/F12 (Thermo Fisher); Neurobasal media (Thermo Fisher) (1:1), 1:100 N2 supplement (Gibco), 1:50 B27 without Vitamin A (Gibco), 1% GlutaMAX (Gibco), 1% minimum essential media-essential amino acid (MEM-NEAA) (Gibco), 0.1% β -

mercaptoethanol (Gibco) supplemented with 1 $\mu\text{g}/\text{mL}$ heparin (Merck), 10 μM SB431542 (Miltenyi), 200 ng/mL human Noggin (Miltenyi), 0.8 μM CHIR99021 (R&D) and 10 μM Rock inhibitor Y27632 (R&D)). Following a two-day incubation period, the rock inhibitor was removed, and cells were cultured in NIC media until day 3. On day 4, hMLOs were supplemented with 100 ng/mL SHH-C25II (Miltenyi) and 100 ng/mL human FGF8b (Miltenyi). On day 7, the cells were embedded in 30 μL growth factor reduced matrigel (Merck) for 30 min. at 37 °C and cultured for 24 h in tissue growth induction media (Neurobasal media, 1:100 N2 supplement, 1:50 B27 without vitamin A, 1% GlutaMAX, 1% MEM-NEAA, 0.1% β -mercaptoethanol supplemented with 2.5 $\mu\text{g}/\text{mL}$ insulin, 200 ng/mL mouse laminin, 100 ng/mL SHH-C25II and 100 ng/mL human FGF8b. The following day, hMLOs were transferred into ultra-low-attachment 6-well plates (Corning) containing final differentiation media (Neurobasal media, 1:100 N2 supplement, 1:50 B27 without Vitamin A, 1% GlutaMAX, 1% MEM-NEAA, 0.1% β -mercaptoethanol, 1% Pen/Strep (Gibco), 10 ng/mL BDNF (Miltenyi), 10 ng/mL GDNF (Miltenyi), 100 μM ascorbic acid (Sigma) and 125 μM db-cAMP (Sigma). The hMLOs were cultured on a shaker and medium was changed every three days. hMLOs were treated on day 44 of organoid formation with the respective test compounds for 24 h. At day 45, organoids were harvested for further analysis. RNA isolation, reverse transcription and quantitative real-time PCR (qRT-PCR): Total RNA from hMLOs was isolated using TRIzol (Invitrogen) following the manufacturer's protocol. RNA extraction was performed using chloroform:isoamyl alcohol (24:1)(Thermo Scientific), precipitated in isopropanol and resuspended in nuclease-free ddH₂O. After DNase digestion, 500 μg total RNA was reverse transcribed using the RevertAid First-strand-cDNA-synthesis kit (Thermo Fisher) and random hexamers following the manufacturer's protocol. qRT-PCR was conducted with specific primers targeting hTH (5'-GCT GGA CAA GTG TCA TCA CCT G-3' (fw) and 5'-CCT GTA CTG GAA GGC GAT CTC A-3' (rev)), Nurr1 (5'-GGC TGA AGC CAT GCC TTG T-3' (fw) and 5'-GTG AGG TCC ATG CTA AAC TTG ACA-3' (rev)) and RNA polymerase 2 (5'-GCA CCA CGT CCA ATG ACA-3' (fw) and 5'-GTC GGC TGC TTC CAT AA-3' (rev)) using the LightCycler® 480 SYBR Green I (Roche) on a Roche LightCycler 480 II qPCR system. Relative gene expression was determined using the $-\Delta\Delta\text{Ct}$ method. All genes were normalized to RNA polymerase II values. Immunostaining of hMLOs: hMLOs were washed twice with PBS and fixed in 4% paraformaldehyde (PFA) overnight at 4 °C. On the following day, hMLOs were washed twice with PBS, cryoprotected and stored in 30% sucrose/PBS. Organoids were sectioned at 25 μm on a cryostat (Leica CM 3050 S, Leica Biosystems, Wetzlar, Germany). Immunostaining was performed within 1.5 mL Eppendorf tubes. Sections were permeabilized in 0.3% Triton X-100, blocked in 5% FBS, 0.1% Triton X-100/PBS and incubated as floating section in 1:200 dilution of primary antibody (rabbit anti-Tyrosine-Hydroxylase, Merck (AB152)) in blocking solution overnight. The next day, sections were washed twice with 0.1% Triton X-100, incubated in 1:500 dilution of secondary antibody (AlexaFluorTM 594 goat anti-rabbit IgG (H + L), Invitrogen) in blocking solution for 1.5 h and Hoechst 33342 (Chem-Cruz) was added in 1:10 000 dilution for 30 min for nuclear staining. Sections were mounted onto glass slides and imaged using a Zeiss LSM 980 microscope (Carl Zeiss AG, Oberkochen, Germany). The staining protocol was adapted from^{60,61}. Images were manually quantified by selecting a fixed area and counting TH+ neurons. The images used for quantification were acquired from four different sections of two different organoids for each condition. Statistical analysis: All experiments were performed at least in triplicate, if not otherwise indicated. Results are expressed as mean \pm SD. Statistical significance was analyzed using two-tailed Student's t-test (* p < 0.05, ** p < 0.01 and *** p < 0.001).

Reporting summary

Further information on research design is available in the Nature Portfolio Reporting Summary linked to this article.

Data availability

All data supporting the results of this study are available from the corresponding author. Source data for Figs. 1, 4, and 5 are provided in Supplementary Data 2.

Received: 28 December 2023; Accepted: 14 June 2024;

Published online: 29 June 2024

References

- Zetterström, R. H., Williams, R., Perlmann, T. & Olson, L. Cellular expression of the immediate early transcription factors Nurr1 and NGFI-B suggests a gene regulatory role in several brain regions including the nigrostriatal dopamine system. *Mol. Brain Res.* **41**, 111–120 (1996).
- Kummari, E., Guo-Ross, S. X., Partington, H. S., Nutter, J. M. & Eells, J. B. Quantitative immunohistochemistry to measure regional expression of Nurr1 in the brain and the effect of the Nurr1 heterozygous genotype. *Front. Neuroanat.* **15**, 563854 (2021).
- Saijo, K. et al. A Nurr1/CoREST pathway in Microglia and Astrocytes protects Dopaminergic neurons from inflammation-induced death. *Cell* **137**, 47–59 (2009).
- Zetterström, R. H. et al. Dopamine neuron agenesis in Nurr1-deficient mice. *Science* **276**, 248–250 (1997).
- Kadkhodaei, B. et al. Nurr1 is required for maintenance of maturing and adult midbrain dopamine neurons. *J. Neurosci.* **29**, 15923–15932 (2009).
- Willems, S. et al. Nurr1 modulation mediates neuroprotective effects of statins. *Adv. Sci.* **9**, e2104640 (2022).
- Chu, Y. et al. Nurr1 in Parkinson's disease and related disorders. *J. Comp. Neurol.* **494**, 495–514 (2006).
- Decressac, M. et al. α -synuclein-induced down-regulation of Nurr1 disrupts GDNF signaling in nigral dopamine neurons. *Sci. Transl. Med.* **4**, 163ra156 (2012).
- Liu, W., Gao, Y. & Chang, N. Nurr1 overexpression exerts neuroprotective and anti-inflammatory roles via down-regulating CCL2 expression in both in vivo and in vitro Parkinson's disease models. *Biochem. Biophys. Res. Commun.* **482**, 1312–1319 (2017).
- Parra-Damas, A. et al. Crtc1 activates a transcriptional program deregulated at early Alzheimer's disease-related stages. *J. Neurosci.* **34**, 5776–5787 (2014).
- Yao, P. L., Parmar, V. M., Choudhary, M. & Malek, G. NURR1 expression regulates retinal pigment epithelial-mesenchymal transition and age-related macular degeneration phenotypes. *Proc. Natl. Acad. Sci. USA.* **119**, e2202256119 (2022).
- Willems, S. & Merk, D. Medicinal chemistry and chemical biology of Nurr1 Modulators: An emerging strategy in neurodegeneration. *J. Med. Chem.* **65**, 9548–9563 (2022).
- Wang, Z. et al. Structure and function of Nurr1 identifies a class of ligand-independent nuclear receptors. *Nature* **423**, 555–560 (2003).
- Willems, S. et al. The orphan nuclear receptor Nurr1 is responsive to non-steroidal anti-inflammatory drugs. *Commun. Chem.* **3**, 85 (2020).
- Yu, X., Shang, J. & Kojetin, D. J. Molecular basis of ligand-dependent Nurr1-RXR α activation. *Elife* **12**, e85039 (2023).
- Bruning, J. M. et al. Covalent modification and regulation of the nuclear receptor Nurr1 by a Dopamine metabolite. *Cell Chem. Biol.* **26**, 674–685.e6 (2019).
- de Vera, I. M. S. et al. Identification of a binding site for unsaturated fatty acids in the orphan nuclear receptor Nurr1. *ACS Chem. Biol.* **11**, 1795–1799 (2016).
- Rajan, S. et al. PGE1 and PGA1 bind to Nurr1 and activate its transcriptional function. *Nat. Chem. Biol.* **16**, 876–886 (2020).
- Munoz-Tello, P. et al. Assessment of NR4A ligands that directly bind and modulate the orphan nuclear receptor Nurr1. *J. Med. Chem.* **63**, 15639–15654 (2020).
- Vietor, J. et al. Development of a potent Nurr1 agonist tool for in vivo applications. *J. Med. Chem.* **66**, 6391–6402 (2023).
- Ballarotto, M. et al. De Novo design of Nurr1 agonists via fragment-augmented generative deep learning in low-data regime. *J. Med. Chem.* **66**, 8170–8177 (2023).
- Sai, M. et al. Structure-guided design of Nurr1 agonists derived from the natural ligand dihydroxyindole. *J. Med. Chem.* **66**, 13556–13567 (2023).
- Stiller, T. & Merk, D. Exploring fatty acid mimetics as NR4A ligands. *J. Med. Chem.* **66**, 15362–15369 (2023).
- Kim, C.-H. et al. Nuclear receptor Nurr1 agonists enhance its dual functions and improve behavioral deficits in an animal model of Parkinson's disease. *Proc. Natl. Acad. Sci.* **112**, 8756–8761 (2015).
- Moon, M. et al. Nurr1 (NR4A2) regulates Alzheimer's disease-related pathogenesis and cognitive function in the 5XFAD mouse model. *Aging Cell* **18**, e12866 (2019).
- De Bruyn, T. et al. Structure-based identification of oap1b1/3 inhibitors. *Mol. Pharmacol.* **83**, 1257–1267 (2013).
- Ren, S. et al. Discovery and characterization of novel, potent, and selective cytochrome P450 2J2 inhibitors. *Drug Metab. Dispos.* **41**, 60–71 (2013).
- Willems, S., Ohmdorf, J., Kilu, W., Heering, J. & Merk, D. Fragment-like chloroquinolineamines activate the orphan nuclear receptor Nurr1 and elucidate activation mechanisms. *J. Med. Chem.* **64**, 2659–2668 (2021).
- Den Braver-Sewradj, S. P. et al. Reduction and scavenging of chemically reactive drug metabolites by NAD(P)H:Quinone Oxidoreductase 1 and NRH:Quinone Oxidoreductase 2 and variability in hepatic concentrations. *Chem. Res. Toxicol.* **31**, 116–126 (2018).
- Qiao, S. et al. The antimalarial amodiaquine causes autophagic-lysosomal and proliferative blockade sensitizing human melanoma cells to starvation- And chemotherapy-induced cell death. *Autophagy* **9**, 2087–2102 (2013).
- Espinoza, J. A. et al. The antimalarial drug amodiaquine stabilizes p53 through ribosome biogenesis stress, independently of its autophagy-inhibitory activity. *Cell Death Differ* **27**, 773–789 (2020).
- Zhang, Y. et al. Glutathione S-transferase P1 protects against Amodiaquine Quinoneimines-induced cytotoxicity but does not prevent activation of endoplasmic reticulum stress in HepG2 cells. *Front. Pharmacol.* **9**, 388 (2018).
- Kim, T. H., Kim, H. K. & Hwang, E. S. Novel anti-adipogenic activity of anti-malarial amodiaquine through suppression of PPAR γ activity. *Arch. Pharm. Res.* **40**, 1336–1343 (2017).
- Baell, J. & Walters, M. A. Chemistry: Chemical con artists foil drug discovery. *Nature* **513**, 481–483 (2014).
- Baell, J. B. & Nissink, J. W. M. Seven year itch: Pan-Assay Interference Compounds (PAINS) in 2017 – Utility and limitations. *ACS Chem. Biol.* **13**, 36–44 (2017).
- Kim, W. et al. An optimized Nurr1 agonist provides disease-modifying effects in Parkinson's disease models. *Nat. Commun.* **14**, 4283 (2023).
- Willems, S. et al. Scaffold hopping from amodiaquine to novel Nurr1 agonist chemotypes via microscale analogue libraries. *ChemMedChem* **17**, e2022000 (2022).
- Kaur, K., Jain, M., Reddy, R. P. & Jain, R. Quinolines and structurally related heterocycles as antimalarials. *Eur. J. Med. Chem.* **45**, 3245–3264 (2010).
- Almaria Garcia, A., Lardenois, P. & Olivier, A. Derivatives of 2-aryl-6-phenyl-imidazo [1, 2-a]pyridines, their preparation and their therapeutic use. WO 2008/034974A1. *Sanofi-Aventis* (2008).
- Lesuisse, D. et al. Development of a novel NURR1/NOT agonist from hit to lead and candidate for the potential treatment of Parkinson's disease. *Bioorg. Med. Chem. Lett.* **29**, 929–932 (2019).
- Smith, G. A. et al. A Nurr1 agonist causes neuroprotection in a Parkinson's disease lesion model primed with the toll-like receptor 3 dsRNA inflammatory stimulant Poly(I:C). *PLoS One* **10**, e0121072 (2015).

42. de Vink, P. J. et al. Cooperativity as quantification and optimization paradigm for nuclear receptor modulators. *Chem. Sci.* **13**, 2744–2752 (2022).
43. Gao, L., Zhou, W., Symmes, B. & Freed, C. R. Re-cloning the N27 dopamine cell line to improve a cell culture model of Parkinson's disease. *PLoS One* **11**, e0160847 (2016).
44. Hartung, I. V., Rudolph, J., Mader, M. M., Mulder, M. P. C. & Workman, P. Expanding chemical probe space: quality criteria for covalent and degrader probes. *J. Med. Chem.* **66**, 9297–9312 (2023).
45. <https://www.thesgc.org/chemical-probes/>.
46. Puech, C. et al. Assessment of HBEC-5i endothelial cell line cultivated in astrocyte conditioned medium as a human blood-brain barrier model for ABC drug transport studies. *Int. J. Pharm.* **551**, 281–289 (2018).
47. Smits, L. M. et al. Modeling Parkinson's disease in midbrain-like organoids. *npj Park. Dis.* **5**, 5 (2019).
48. Kim, H. et al. Modeling G2019S-LRRK2 sporadic Parkinson's disease in 3D midbrain Organoids. *Stem Cell Rep.* **12**, 518–531 (2019).
49. Cookson, M. R. α -Synuclein and neuronal cell death. *Mol. Neurodegener.* **4**, 9 (2009).
50. Pauli, G. F. et al. Importance of purity evaluation and the potential of quantitative ^1H NMR as a purity assay. *J. Med. Chem.* **57**, 9220–9231 (2014).
51. Gellrich, L. et al. L-Thyroxin and the nonclassical thyroid hormone TETRAC are potent activators of PPAR γ . *J. Med. Chem.* **63**, 6727–6740 (2020).
52. Pollinger, J. et al. Tuning nuclear receptor selectivity of Wy14,643 towards selective Retinoid X receptor modulation. *J. Med. Chem.* **62**, 2112–2126 (2019).
53. Rau, O. et al. Carnosic acid and carnosol, phenolic diterpene compounds of the labiate herbs rosemary and sage, are activators of the human peroxisome proliferator-activated receptor gamma. *Planta Med.* **72**, 881–887 (2006).
54. Flesch, D. et al. Non-acidic farnesoid X receptor modulators. *J. Med. Chem.* **60**, 7199–7205 (2017).
55. Schmidt, J. et al. NSAIDs Ibuprofen, Indometacin, and Diclofenac do not interact with Farnesoid X Receptor. *Sci. Rep.* **5**, 14782 (2015).
56. Heitel, P. et al. Computer-assisted discovery and structural optimization of a novel Retinoid X receptor agonist chemotype. *ACS Med. Chem. Lett.* **10**, 203–208 (2019).
57. Seuter, S., Väisänen, S., Rådmark, O., Carlberg, C. & Steinhilber, D. Functional characterization of vitamin D responding regions in the human 5-Lipoxygenase gene. *Biochim. Biophys. Acta* **1771**, 864–872 (2007).
58. Sugano, K., Hamada, H., Machida, M. & Ushio, H. High throughput prediction of oral absorption: improvement of the composition of the lipid solution used in parallel artificial membrane permeation assay. *SLAS Discov* **6**, 189–196 (2001).
59. Jo, J. et al. Midbrain-like Organoids from human Pluripotent stem cells contain functional Dopaminergic and Neuromelanin-producing neurons. *Cell Stem Cell* **19**, 248–257 (2016).
60. Cederquist, G. Y. et al. Specification of positional identity in forebrain organoids. *Nat. Biotechnol.* **37**, 436–444 (2019).
61. Watanabe, M. et al. Self-organized cerebral organoids with human-specific features predict effective drugs to combat Zika virus infection. *Cell Rep* **21**, 517–532 (2017).
62. Hopkins, A. L., Keseru, G. M., Leeson, P. D., Rees, D. C. & Reynolds, C. H. The role of ligand efficiency metrics in drug discovery. *Nat. Rev. Drug Discov.* **13**, 105–121 (2014).
63. RDKit: Open-source cheminformatics. Open-source cheminformatics. <http://www.rdkit.org>.

Acknowledgements

This research was co-funded by the European Union (ERC, NeuRoPROBE, 101040355). Views and opinions expressed are however those of the author(s) only and do not necessarily reflect those of the European Union or the European Research Council. Neither the European Union nor the granting authority can be held responsible for them. Further support was provided by Deutsche Forschungsgemeinschaft (DFG) (GRK2668 (435874434); 496872373; 498956525; 497803923). The authors thank Jason Tchieu for sharing the iPSC-LRRK2 isogenic control and iPSC-LRRK2-G2019S cell lines.

Author contributions

M.S. and D.M. conceived the project. M.S. performed the chemical synthesis. M.S., E.C.H., H.T., T.K., M.L., M.V. and J.A.M. performed the biological experiments. All authors were involved in the interpretation of results. D.M. supervised the project and wrote the manuscript with contributions from all authors.

Funding

Open Access funding enabled and organized by Projekt DEAL.

Competing interests

M.S. and D.M. are inventors of the European patent application EP24155686: "Nurr1 modulators" claiming compounds described in this study. There are no other conflicts to declare.

Additional information

Supplementary information The online version contains supplementary material available at <https://doi.org/10.1038/s42004-024-01224-0>.

Correspondence and requests for materials should be addressed to Daniel Merk.

Peer review information *Communications Chemistry* thanks Diwan Rawat, John Spencer, and the other, anonymous, reviewer(s) for their contribution to the peer review of this work.

Reprints and permissions information is available at <http://www.nature.com/reprints>

Publisher's note Springer Nature remains neutral with regard to jurisdictional claims in published maps and institutional affiliations.

Open Access This article is licensed under a Creative Commons Attribution 4.0 International License, which permits use, sharing, adaptation, distribution and reproduction in any medium or format, as long as you give appropriate credit to the original author(s) and the source, provide a link to the Creative Commons licence, and indicate if changes were made. The images or other third party material in this article are included in the article's Creative Commons licence, unless indicated otherwise in a credit line to the material. If material is not included in the article's Creative Commons licence and your intended use is not permitted by statutory regulation or exceeds the permitted use, you will need to obtain permission directly from the copyright holder. To view a copy of this licence, visit <http://creativecommons.org/licenses/by/4.0/>.

© The Author(s) 2024